

Evaluating Climate Models with Sliced Elastic Distance

Robert C. Garrett¹, Trevor Harris², Bo Li¹

July 18, 2023

Abstract

The validation of global climate models plays a crucial role in ensuring the accuracy of climatological predictions. However, existing statistical methods for evaluating differences between climate fields often overlook time misalignment and therefore fail to distinguish between sources of variability. To more comprehensively measure differences between climate fields, we introduce a new vector-valued metric, the sliced elastic distance. This new metric simultaneously accounts for spatial and temporal variability while decomposing the total distance into shape differences (amplitude), timing variability (phase), and bias (translation). We compare the sliced elastic distance against a classical metric and a newly developed Wasserstein-based approach through a simulation study. Our results demonstrate that the sliced elastic distance outperforms previous methods by capturing a broader range of features. We then apply our metric to evaluate the historical model outputs of the Coupled Model Intercomparison Project (CMIP) members, focusing on monthly average surface temperatures and monthly total precipitation. By comparing these model outputs with quasi-observational ERA5 Reanalysis data products, we rank the CMIP models and assess their performance. Additionally, we investigate the progression from CMIP phase 5 to phase 6 and find modest improvements in the phase 6 models regarding their ability to produce realistic climate dynamics.

Keywords: Amplitude; Climate data products; Distance metric; Functional data; Phase; Spatiotemporal fields

¹Department of Statistics, University of Illinois at Urbana-Champaign

²Department of Statistics, Texas A&M University

1 Introduction

General Circulation Models (GCMs), or climate models, are mathematical representations of the climate system that describe the interactions between matter and energy through the ocean, atmosphere, and land (Washington and Parkinson, 2005). Climate models are the primary tool for investigating the response of the climate system to changes in forcing, such as increases in CO₂, and for projecting future climate states (Flato et al., 2014). They are also important tools for understanding and projecting climate behavior on seasonal, annual, decadal, and centennial time scales. To assess the accuracy of climate models for these essential tasks, climate scientists compare the output of model simulations against observational data (Rood, 2019). This has led to a proliferation of climate model validation techniques for ensuring that climate models capture the dynamics of the climate system (Roca et al., 2021).

The Coupled Model Intercomparison Project (CMIP) was initiated in 1995 as a comprehensive and systematic program for assessing climate models against each other and observational data (Eyring et al., 2016). CMIP helps to understand natural, unforced variability and the response of the climate system to changes in radiative forcings using multi-model ensembles. Each model in CMIP participates in a wide variety of experiments such as performing a historical simulation, a pre-industrial control simulation, and various simulations representing different scenarios for CO₂ emissions (Eyring et al., 2016). Under the historical forcing scenario, climate models are initialized with the estimated climatic conditions of 1850CE, when wide-scale temperatures were first recorded, and run through 2015CE. Because historical simulations coincide with observational measurements, we can validate each model’s projected climate against observational data or quasi-observational data products (Raäisaänen, 2007), to assess their reconstructive skill. Comparing historical models to reanalysis data, which is observational data but gap-filled via data assimilation, has become one

popular climate model validation method (Flato et al., 2014).

There are many quantitative methods for comparing two datasets that have been applied to assess the similarity between climate model output and reanalysis fields. The most common approach is to compute the $L2$ distance, or root mean square error (RMSE), between different features of the climate model output and the reanalysis field (Li et al., 2021; Zamani et al., 2020; Karim et al., 2020; Ayugi et al., 2021). RMSE provides a direct calculation of the differences between climate fields but does not distinguish sources of variability such as bias and timing variability. Another approach, which is invariant to the bias between two fields, is to compute measures of correlation between climate model output and reanalysis fields (Zhao et al., 2021; Zamani et al., 2020; Karim et al., 2020; Ayugi et al., 2021).

More comprehensive approaches use the wavelet decomposition of spatial processes (Briggs and Levine, 1997; Shen et al., 2002; Cressie et al., 2008) to compare the spatial-frequency content of two fields. Other approaches measure the loss differential between models of random processes (Snell et al., 2000; Wang et al., 2007; Hering and Genton, 2011) or compare the empirical moments (Lund and Li, 2009; Li and Smerdon, 2012) of each field to assess their mean and dependency structure. Finally, researchers have introduced functional data analysis (FDA) techniques for comparing spatial and spatiotemporal random fields, considering the random fields as continuous functions. Many of these approaches compare the underlying mean functions from two sets of functional data (Ramsay and Silverman, 2005; Zhang and Chen, 2007; Horváth et al., 2013; Staicu et al., 2014). Other approaches include the second-order structure in the comparison (Zhang and Shao, 2015; Li et al., 2016), or compare the distributions of two spatial random processes (Harris et al., 2021).

Despite these recent advancements, current methods have so far not considered possible time misalignment between two spatiotemporal random fields. Such mis-

alignment often exhibits in climate models regarding the timing of seasonal transitions and climate events such as El Niño and spring snow melt in the Arctic (Bindoff et al., 2014). Methods that do not consider temporal alignment are known as “cross-sectional” because they consider two spatiotemporal fields as directly comparable at each time point. This limitation compromises the ability of cross-sectional metrics to accurately compare climate models to observed data and reanalysis because variability due to time misalignment is misattributed to differences in the underlying climate dynamics. Recognizing such issues, Vissio et al. (2020) proposed a Wasserstein distance-based method to compare distributions of climate variables. This Wasserstein-based method finds the optimal pairing between observations from two spatiotemporal fields to minimize the euclidean norm, so it breaks the time matching limitation of cross-sectional methods. However, these optimal pairings do not preserve temporal ordering, which is an essential characteristic of temporal trajectories of climate variables.

Shape differences have emerged to be an effective measure to characterize deviation of the trajectory, or dynamical evolution, of the climate model compared with the reanalysis fields, irrespective of its systematic bias or mistiming of events (Bindoff et al., 2014). Two trajectories with identical shapes have the exact same underlying dynamics, and we can decompose any observed differences into shape differences, phase differences, and biases using elastic functional data analysis (Joshi et al., 2007). Due to these nice properties, shape differences may measure the discrepancies between climate models and reanalysis products more appropriately. Figure 1 provides an intuitive comparison of cross-sectional, Wasserstein-based, and elastic functional data analysis methods for comparing univariate time series.

To create a tailored tool for climate model evaluation, we propose a sliced elastic distance metric that separates shape differences, or differences in the underlying dynamics of climate trajectories, from errors due to time misalignment and bias. Our

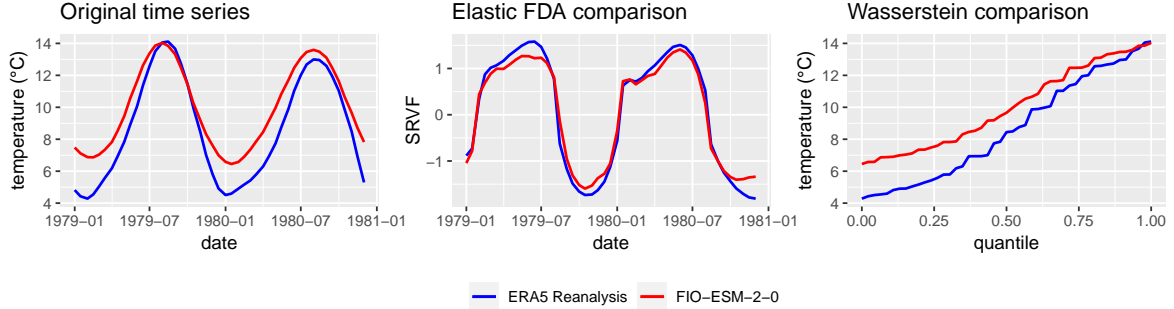


Figure 1: Demonstration of three methods for comparing time series of climate data. The leftmost panel shows monthly average (2m) surface temperature values for the west coast of British Columbia, Canada, from January 1979 to December 1980. Curves are provided for both the ERA5 Reanalysis dataset and FIO-ESM-2-0 climate model output. Cross-sectional metrics directly compare the raw time series (left), elastic FDA first removes bias and phase variability from the time series using the process described in Section 3.1 and then compares the shape of the aligned data (middle), and Wasserstein distance compares the time series after reordering them to obtain the empirical quantiles (right). Unlike elastic functional data analysis, Wasserstein distance is not invariant to bias and does not uphold the temporal ordering of the data.

approach, based on the elastic functional data analysis framework (Joshi et al., 2007; Srivastava and Klassen, 2016), computes amplitude, phase, and translation distances for convolutional projections from climate fields, called slices. Compared to previous cross-sectional approaches and the Wasserstein-based approach from Vissio et al. (2020), the sliced elastic distance accounts for more spatial and temporal information when comparing climate models against reanalysis data, resulting in a comprehensive and more robust evaluation. We apply our distance metric to rank climate models as well as assess the progression of the new CMIP era with respect to monthly average surface temperature and monthly total precipitation.

The rest of the article is organized as follows. Section 2 describes the climate data for our analysis. Section 3 proposes the sliced elastic distance, establishes its theoretical properties, and details the method implementation. Section 4 demonstrates the performance of the sliced elastic distance on simulated model validation scenarios. Section 5 applies our distance metric to evaluate the CMIP models and compares the two eras of CMIP. Section 6 provides a brief discussion of the method and the results.

2 Data Description

Historical climate model simulations have evolved over time thanks to the constant efforts made to improve climate models. We consider climate model outputs from the Coupled Model Intercomparison Project (CMIP) phases 5 and 6, available at <https://esgf-node.llnl.gov/projects/esgf-llnl/>, to assess the general performance of CMIP models. This additionally allows us to assess the progression from phase 5 to 6. We consider both the monthly average near-surface (2m) temperature in degrees Celsius and monthly total precipitation in mm for climate model validation. The CMIP6 historical simulations are organized by ensembles, each of which is distinguished with an `ripf` identifier, representing realization, initialization, physics, and forcings of the model, respectively (Eyring et al., 2016). CMIP5 has a similar organization but is indexed by `rip`. We obtain 48 model outputs with the `r1i1p1f1` variant ID from CMIP6 and 37 model outputs with the `r1i1p1` ID from CMIP5. All 37 CMIP5 models have both surface temperature and precipitation output available. Although all 48 CMIP6 models have surface temperature output available, only 28 have precipitation output available.

We collect the European Centre for Medium-Range Weather Forecasts (ECMWF) Reanalysis 5th Generation (ERA5) (Hersbach et al., 2020) as the reference for climate

model evaluation. Data were obtained from the ERA5 monthly mean data on single levels from 1940 to present (Hersbach et al., 2023) on the Copernicus Climate Data Store website: <https://cds.climate.copernicus.eu/cdsapp#!/dataset/reanalysis-era5-single-levels-monthly-means?tab=overview>. Following Vissio et al. (2020), we also include Reanalysis-2 data from the National Centers for Environmental Protection (NCEP) in our analysis to assess variability between reanalysis data products relative to the discrepancies between ERA5 and CMIP models. The NCEP Reanalysis-2 data are available at <https://ps1.noaa.gov/data/gridded/data.ncep.reanalysis2.html>. The two reanalysis datasets contain both the monthly temperature and precipitation.

Each data product has the climate variables on a regular latitude-longitude grid across the globe. The grid size varies for different data products. See Appendix A for full details on the spatial resolution of each CMIP output and reanalysis dataset. All model evaluation is conducted during the historical period of January 1979 to November 2005, a common period covered by ERA5, NCEP, and many CMIP5 and CMIP6 models.

3 Methods

3.1 Review of elastic functional data analysis

Elastic functional data analysis (EFDA) (Joshi et al., 2007; Tucker et al., 2013; Srivastava and Klassen, 2016) is a framework for comparing the shapes of absolutely continuous manifold-valued functions parameterized by time. To serve our climate model validation approach, we consider a special case of functions in the space $\mathcal{F}_{\mathcal{T}}$, the set of absolutely continuous functions from $\mathcal{T} \mapsto \mathbb{R}$. The time domain \mathcal{T} is assumed to be $[0, 1]$ without loss of generality. To compare the shapes of two functions

$f(t), g(t) \in \mathcal{F}_{\mathcal{T}}$, EFDA uses time warping to decompose the variability between f and g into amplitude, phase, and translation distances. On the space $\mathcal{F}_{\mathcal{T}}$, each of the three distances alone are not valid distance metrics because they do not individually satisfy the positivity property of a metric: for all $f, g \in \mathcal{F}_{\mathcal{T}}$, $f \neq g \Rightarrow D(f, g) > 0$, where $D(f, g)$ denotes a distance between f and g .

To create proper amplitude, phase, and translation metrics, EFDA instead introduces the square root velocity function (SRVF) representation (Joshi et al., 2007) along with time warping to decompose functional data into three component spaces. The SRVF of a function $f \in \mathcal{F}_{\mathcal{T}}$ is defined as $q_f(t) = \text{sign}(\dot{f}(t))\sqrt{|\dot{f}(t)|}$ (Srivastava and Klassen, 2016), where $\dot{f}(t)$ is the derivative of $f(t)$ with respect to time t . Because q_f is an element of \mathbb{L}_2 , the set of square-integrable functions, it is a unique and invertible representation of f up to the intercept $f(0)$. We then use $\gamma_f(t) \in \Gamma$ to denote a warping function for q_f , where Γ is the set of functions on \mathcal{T} which are boundary preserving, absolutely continuous, and weakly increasing. Let D_A , D_P , and D_T denote the valid amplitude, phase, and translation distance metrics between f and g , respectively. Srivastava and Klassen (2016) defines these three distances as follows:

$$\begin{aligned} D_A(f, g) &= \inf_{\gamma_f, \gamma_g \in \Gamma} \|(q_f, \gamma_f) - (q_g, \gamma_g)\|_2, \\ D_P(f, g) &= \cos^{-1} \left(\int_0^1 \sqrt{\dot{\gamma}_f^*(t)} \sqrt{\dot{\gamma}_g^*(t)} dt \right), \\ D_T(f, g) &= |f(0) - g(0)|, \end{aligned} \tag{3.1}$$

where $(q_f, \gamma) = (q_f(\gamma(t)))\sqrt{\dot{\gamma}}$ is the SRVF of $f(\gamma(t))$, the time warping of f by γ , and $\dot{\gamma}$ is the derivative of γ with respect to time. Phase distance between f and g is defined as a function of their relative phase functions, denoted by γ_f^* and γ_g^* , which are the minimizers obtained in the calculation of $D_A(f, g)$. The values $f(0)$ and $g(0)$ are the time intercepts of each function. The distance functions D_A , D_P , and D_T are all proper metrics on a different space from the SRVF representation (Srivastava

and Klassen, 2016). Amplitude distance is a metric on the quotient space \mathbb{L}_2/Γ and provides a comparison of q_f and q_g after accounting for phase variability. Phase distance is a metric on Γ , and quantifies the severity of the time warping required to align q_f and q_g . Translation distance is a metric on \mathbb{R} and represents the magnitude of the difference between the intercepts of each function.

The triplet of amplitude, phase, and translation distance together is called the elastic distance, denoted as:

$$D_E(f, g) = \left[D_A(f, g), D_P(f, g), D_T(f, g) \right]^T, \quad (3.2)$$

where x^T refers to the transpose of a row vector x . Even though D_A , D_P , and D_T are metrics on different spaces, when considered jointly, they fully characterize the differences between two functions. In fact, Section 3.3 proves that D_E is a vector-valued metric (Sastry et al., 2012) on the space $\mathcal{F}_{\mathcal{T}}$. EFDA centers on identifying the elastic distance between functions.

3.2 Sliced elastic distances

Spatiotemporal climate fields can be viewed as functional data indexed by spatial location s and time t , denoted by $f(s, t) \in \mathcal{F}_{\mathcal{S} \times \mathcal{T}}$, where $\mathcal{F}_{\mathcal{S} \times \mathcal{T}}$ is the set of absolutely continuous functions from $\mathcal{S} \times \mathcal{T} \mapsto \mathbb{R}$. The spatial domain \mathcal{S} is the Earth’s surface, which is indexed by latitude and longitude coordinates from the unit sphere \mathbb{S}^2 . The time domain \mathcal{T} is the historical period of January 1979 to November 2005, represented by the interval $[0, 1]$. To simplify notation, we will suppress (s, t) from $f(s, t)$ unless there is a risk of confusion.

Although such data can be considered as multivariate functions of time so that traditional EFDA methods may apply (Joshi et al., 2007; Srivastava and Klassen, 2016), there are two main issues with this approach. Firstly, traditional EFDA necessitates

that the functions being compared have a shared set of p dimensions, translating to a requirement that each climate model output and reanalysis product share a common spatial grid. However, in practice, the size and structure of the spatial grid often varies between data products. Secondly, traditional EFDA does not account for spatial variability and allows only a single warping function to align two p -variate functional data (Srivastava and Klassen, 2016; Joshi et al., 2007; Bernal et al., 2021; Tucker et al., 2022; Hartman et al., 2021). Whereas, climate fields exhibit spatially-varying phase characteristics such as seasonal transitions varying by latitude as well as alternating in the northern and southern hemispheres. Our framework instead treats \mathcal{S} as part of the function domain, naturally integrating spatial information into the data. This enables our method to combine data from nearby locations while simultaneously allowing time warping to vary at different locations, thereby accounting for phase variability in different regions of the globe.

Inspired by the sliced Wasserstein distance (Rabin et al., 2011; Manole et al., 2022) proposed for high-dimensional distributions, we introduce a sliced elastic distance to compare two spatiotemporal fields. Slices are typically constructed as low-dimensional projections of the data. Considering the various grid sizes and structures of different climate data products, we propose to construct slices at arbitrary locations by convolving nearby functional data using a kernel function centered at each slice location. Specifically, we define the slice function, $f_s(t)$, of $f(u, t) \in \mathcal{F}_{S \times T}$ at location $s \in \mathcal{S}$ as

$$f_s(t) = \int_{\mathcal{S}} f(u, t) k_s(u; \theta) du, \quad (3.3)$$

where $k_s(u; \theta)$ is a spatial kernel function with parameter θ centered at location s . The kernel can be any spatially continuous function with a positive spectral density on \mathcal{S} . Analogously, we can define the slice function $g_s(t)$ for $g(u, t) \in \mathcal{F}_{S \times T}$. It is easy to compute $D_E(f_s, g_s)$ as both f_s, g_s are univariate functional data. We then calculate the sliced elastic distance between the two spatiotemporal fields based on

the pairwise elastic distances between the slice functions at each location in \mathcal{S} .

Definition 3.1 (Sliced elastic distance). Let $f, g \in \mathcal{F}_{\mathcal{S} \times \mathcal{T}}$. We define the sliced elastic distance, D_{SE} , between f and g to be the vector consisting of three components: sliced amplitude distance (D_{SA}), sliced phase distance (D_{SP}), and sliced translation distance (D_{ST}):

$$D_{SE}(f, g) = \begin{bmatrix} D_{SA}(f, g) \\ D_{SP}(f, g) \\ D_{ST}(f, g) \end{bmatrix} = \begin{bmatrix} \left\{ \int_{\mathcal{S}} D_A(f_s, g_s)^2 ds \right\}^{1/2} \\ \left\{ \int_{\mathcal{S}} D_P(f_s, g_s)^2 ds \right\}^{1/2} \\ \left\{ \int_{\mathcal{S}} D_T(f_s, g_s)^2 ds \right\}^{1/2} \end{bmatrix}, \quad (3.4)$$

where f_s and g_s are the slices defined in (3.3) and D_A , D_P , and D_T are amplitude, phase, and translation distances between two univariate functions as defined in (3.1).

Since D_{SA} is calculated via the amplitude distance between slices f_s and g_s at each location $s \in \mathcal{S}$, time warping is allowed to vary over space. According to (3.1), the amplitude distance is based on the derivative of each slice. Thus, D_{SA} integrates local differences between the dynamics of two climate fields. The phase distance between f_s and g_s represents the severity of the warping required to align the SRVFs of f_s and g_s . When comparing climate fields, $D_P(f_s, g_s)$ quantifies differences in the timing of weather events and seasonal changes at location s , and $D_{SP}(f, g)$ measures the average time misalignment between the two climate fields. Sliced translation distance only captures differences between two functions at $t = 0$. Though it is a necessary component to ensure that the sliced elastic distances satisfy the properties of a vector-valued metric, it is of little scientific interest for climate field comparison. We will focus on D_{SA} and D_{SP} in what follows.

The sliced elastic distance allows us to compare high-dimensional spatiotemporal data through one-dimensional slices indexed by spatial locations. Each slice represents one perspective of the data with amplitude and phase distances calculated

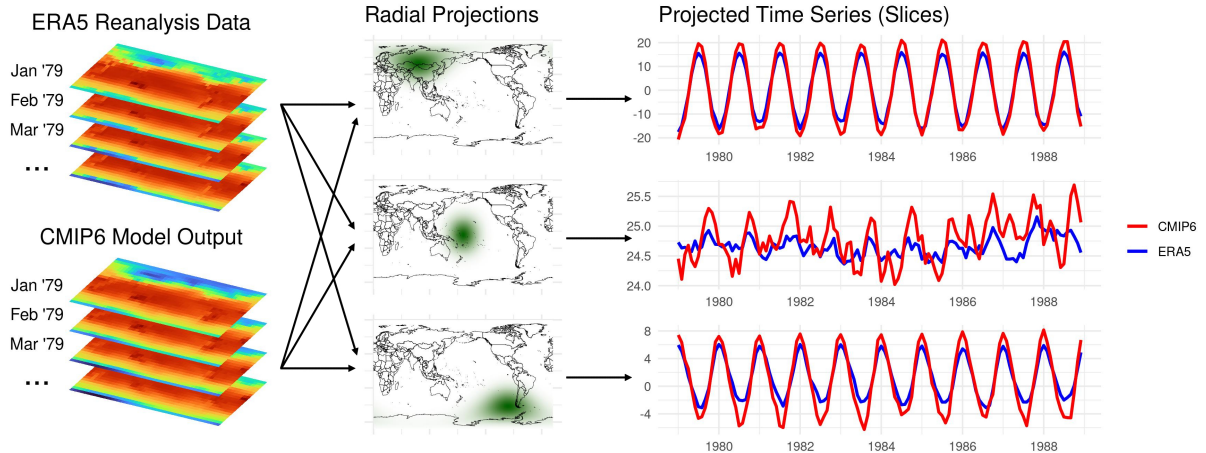


Figure 2: Diagram illustrating how to use sliced elastic distance to compare CMIP6 climate models with ERA5 Reanalysis data. For each month in the historical period, spatial fields from the ERA5 Reanalysis and each CMIP6 climate model are converted into univariate time series using a set of kernel projections. The resulting time series, called slice functions, are then used to compare each CMIP6 model to the ERA5 Reanalysis via the elastic distance metric (3.1). The sliced elastic distance is calculated as the mean of the elastic distances over all kernel projections.

using the usual dynamic programming algorithm (Joshi et al., 2007), therefore avoiding computational concerns with the time alignment step for multivariate functional data (Bernal et al., 2021; Tucker et al., 2022; Hartman et al., 2021). Together, the slices provide a comprehensive view of a spatiotemporal field. Figure 2 illustrates the idea of climate fields comparison using sliced elastic distance. Compared to the method in Vissio et al. (2020) which reduces the climate fields at each time into a single spatial mean, essentially representing the whole field by one single slice, our kernel convolution-based slices capture substantially more spatial variability. Kernel convolution also allows for the comparison of climate model output and reanalysis fields that are available at different spatial resolutions.

Valid choices of kernel functions include the Kent distribution function (Kent,

1982; Heaton et al., 2014) and the generalized Wendland functions (Wendland, 1998; Hubbert and Jäger, 2023). Compact kernels are desirable for our application because they ensure each slice represents climate features in a relatively small local neighborhood, though ultimately providing a global spatial characterization of the misalignment between two fields. We thus choose the Wendland kernel function as in Nychka et al. (2015):

$$k_s(u; r) = \begin{cases} \left(1 - \frac{|s-u|}{r}\right)^6 \left(35 \frac{|s-u|^2}{r^2} + 18 \frac{|s-u|}{r} + 3\right) / 3 & |s-u| \leq r, \\ 0 & |s-u| > r, \end{cases} \quad (3.5)$$

where r is a range parameter determining how compact the function is. In our application, $|s-u|$ is the chordal distance between locations s and u on the Earth, represented as latitude-longitude coordinates. Chordal distance is chosen for theoretical convenience and it approximates the great circle distance when the range parameter is small. Suppose the range parameter is chosen to be smaller than or equal to the diameter of the Earth. In that case, the Wendland functions will be positive definite on \mathbb{S}^2 (Hubbert and Jäger, 2023), therefore meeting the assumptions in Definition 3.1. We will study the role that r plays and the sensitivity of our results to this parameter in Section 4.1.

3.3 Theoretical properties

We first show that the elastic distance $D_E(f(t), g(t))$ defined in (3.1) is a valid vector-valued metric on $\mathcal{F}_{\mathcal{T}}$ and then establish our main result that the sliced elastic distance $D_{SE}(f(s, t), g(s, t))$ is a valid vector-valued metric on $\mathcal{F}_{\mathcal{S} \times \mathcal{T}}$. Both results rely on the idea of vector-valued metric spaces (Sastry et al., 2012; Rao, 2015; Jachymski and Klima, 2016) defined below, which generalize the concept of metric spaces to allow for multiple distance functions.

Definition 3.2 (Vector-valued metric). Let X be a nonempty set, and let $D : X \times X \rightarrow \mathbb{R}^m$ be a length m vector-valued function with the following properties:

1. Identity: $D(x, x) = 0_m$ for all $x \in X$,
2. Symmetry: $D(x, y) = D(y, x)$ for all $x, y \in X$,
3. Triangle Inequality: $D(x, y) \leq D(x, z) + D(z, y)$ for all $x, y, z \in X$,
4. Positivity: $0_m \leq D(x, y)$ for all $x, y \in X$ such that $x \neq y$,

where 0_m is the zero vector of length m , and $a \leq b$ for $a, b \in \mathbb{R}^m$ holds if and only if $a_i \leq b_i$ for all $i \in 1, \dots, m$. We say D is a vector-valued metric with m components and (X, D) is a vector-valued metric space.

Jachymski and Klima (2016) introduced an alternate characterization of vector-valued metrics which states that (X, D) is a vector-valued metric space if and only if D is a family of pseudometrics (D_1, \dots, D_m) such that for any $x, y \in X$, $x \neq y \Rightarrow D_i(x, y) > 0$ for some $i \in 1, \dots, m$. This characterization fits naturally with the EFDA representation. Section 3.1 reviews the three components of EFDA: amplitude, phase, and translation distance. Each is a valid metric on a different space, but not on the original functional data space, $\mathcal{F}_{\mathcal{T}}$. However, it is obvious that if two functions $f(t)$ and $g(t)$ are not the same, there will be a disparity in either their aligned SRVFs, their relative phase functions, or their intercepts, leading to a positive value for the respective amplitude, phase, or translation distance. We use the characterization of vector-valued metrics from Jachymski and Klima (2016) along with properties from Srivastava and Klassen (2016) to prove the following Lemma.

Lemma 3.1. $D_E(f(t), g(t))$ is a vector-valued metric on $\mathcal{F}_{\mathcal{T}}$.

The proof of Lemma 3.1 is deferred to the Appendix B. Based on this result, we show that the sliced elastic distance D_{SE} is a vector-valued metric on $\mathcal{F}_{S \times \mathcal{T}}$.

Theorem 3.2. *If $D = [D_1, \dots, D_m]^T$ is a vector-valued metric on $\mathcal{F}_{\mathcal{T}}$, and $f_s(t)$ and $g_s(t)$ are respectively the slice functions of $f(u, t) \in \mathcal{F}_{\mathcal{S} \times \mathcal{T}}$ and $g(u, t) \in \mathcal{F}_{\mathcal{S} \times \mathcal{T}}$ using a spatially continuous kernel $k(u; \theta)$ with an positive spectral density on \mathcal{S} as defined in (3.3), then the vector-valued function $D_S = [D_{S1}, \dots, D_{Sm}]^T$ with each component defined as*

$$D_{Si}(f, g) = \left\{ \int_{\mathcal{S}} D_i (f_s, g_s)^2 ds \right\}^{1/2}, \quad i = 1, \dots, m,$$

is a vector-valued metric on $\mathcal{F}_{\mathcal{S} \times \mathcal{T}}$.

Corollary 3.3. *The sliced elastic distance $D_{SE}(f(s, t), g(s, t))$ is a vector-valued metric on $\mathcal{F}_{\mathcal{S} \times \mathcal{T}}$.*

Proof of Theorem 3.2 is provided in Appendix B. The proof relies on the convolution theorem for finite-dimensional unit spheres (Driscoll and Healy, 1994; Dokmanic and Petrinovic, 2009) as well as Lemmas B.1 and B.2. Lemma B.1 states that the slicing operation in (3.3) creates valid functional data in $\mathcal{F}_{\mathcal{T}}$ and Lemma B.2 states that pseudometrics on $\mathcal{F}_{\mathcal{T}}$ extend to pseudometrics on $\mathcal{F}_{\mathcal{S} \times \mathcal{T}}$ when our slicing method is applied. Corollary 3.3 follows directly from Lemma 3.1 and Theorem 3.2. Since the sliced elastic distance is a vector-valued metric on $\mathcal{F}_{\mathcal{S} \times \mathcal{T}}$, its components, sliced amplitude, sliced phase, and sliced translation distance, form a suite of metrics that extend the elastic distance to produce a comprehensive comparison of spatiotemporal fields. While our theoretical results are shown for spatial data with a spherical domain such as the Earth’s surface, similar results can be proven for any spatial domain on which a comparable convolution theorem is available.

3.4 Implementation

Because climate model output and reanalysis data products are discrete in both the space and time dimensions, the exact integrals in Definition 3.1 cannot be computed.

We approximate these integrals with summations and averages over a discrete set of locations. One caveat about averaging global data is that data at different coordinates carry drastically different weights due to uneven grid cell areas in regular latitude-longitude grids. To account for this spatial disparity, we use the weighted average detailed below.

It is the user’s decision to choose locations at which they want to have the slice functions. This choice may depend on the grid density of data products and preferences for the spatial resolution of slice locations. In our simulation and data analysis, we choose a regular latitude-longitude grid, G , resolved by 48 latitude values and 96 longitude values, to represent the spatial domain. The resolution of G is chosen to match the lowest resolution among the CMIP models, but users can make their own choice for the grid size and structure. Given the two climate fields represented by $f(u, t) \in \mathcal{F}_{S \times \mathcal{T}}$ and $g(u, t) \in \mathcal{F}_{S \times \mathcal{T}}$ and the common grid G , the sliced elastic distance between f and g can be easily obtained through the following major steps:

1. **Slices** Compute the slice functions f_s and g_s for each location $s \in G$ through location wise multiplication of $f(u, t)$ and $g(u, t)$ with the kernel $k_s(u)$ at each time point. To ensure the temporal sampling rate of f_s and g_s is sufficient for time warping, we estimate a continuous function from each slice by fitting cubic smoothing splines. The smoothing parameter for each slice is chosen via the generalized cross-validation criteria.
2. **Elastic distance** At each location $s \in G$, compute amplitude and phase distances $D_A(f_s, g_s)$ and $D_P(f_s, g_s)$ using the dynamic programming algorithm provided in R package `fdasrvf` (Tucker, 2020).
3. **Spatial weights** Assign weights for each location $s \in G$, denoted as w_s , as the cosine of its latitude to adjust for the different areas of each grid cell. This

follows the standard practice for global climate data, e.g., Li et al. (2016).

4. **Sliced elastic distance** Compute the approximate sliced elastic distance \tilde{D}_{SE} between f and g as follows:

$$\tilde{D}_{SE}(f, g) \approx \left[\begin{array}{c} \left\{ \tilde{w} \sum_{s \in G} w_s D_A(f_s, g_s)^2 \right\}^{1/2} \\ \left\{ \tilde{w} \sum_{s \in G} w_s D_P(f_s, g_s)^2 \right\}^{1/2} \\ \left\{ \tilde{w} \sum_{s \in G} w_s |f_s(0) - g_s(0)|^2 \right\}^{1/2} \end{array} \right], \quad (3.6)$$

where $\tilde{w} = 1 / \sum_{s \in G} w_s$.

In step 2, an adaptation was made to the code in `fdasrvf` for computational efficiency. We observed that in our application to climate model evaluation, time warping of a magnitude greater than six months rarely occurred. So, we apply an additional restriction to the dynamic programming algorithm to keep the time warping within a conservative 12-month window. This restriction on the search space drastically improves computational efficiency.

4 Simulations

We perform simulation studies to evaluate the skill of the sliced elastic distance in distinguishing and quantifying the amplitude and phase discrepancies between two spatiotemporal fields, investigate the influence of the range parameter in the kernel function, and compare our approach with previous methods.

4.1 Assessing the skill of the sliced elastic distance

To make our simulations realistic, we use the first year (January-December 1979) ERA5 Reanalysis (2m) surface air temperature dataset as the baseline data $f(s, t)$. We then generate $g(s, t)$ by applying a series of spatially-varying amplitude and phase

modifications on $f(s, t)$. Let $a_i(s)$, $i = 1, 2, 3$ and $p_j(s)$, $j = 1, 2, 3$ be the sets of parameters used for the amplitude and phase modifications, and let $g_{i,j}(s, t)$ denote the modified versions of ERA5 corresponding to parameters $a_i(s)$ and $p_j(s)$. We obtain $g_{i,j}(s, t)$ by transforming $f(s, t)$ for all $s \in \mathbb{S}^2$ as follows:

$$g_{i,j}(s, t) = a_i(s) \left\{ f \left(s, t + p_j(s) \frac{\sin(2\pi t)}{2\pi} \right) - \int_0^1 f(s, t) dt \right\} + \int_0^1 f(s, t) dt. \quad (4.1)$$

The integral $\int_0^1 f(s, t) dt$ provides the temporal mean of the ERA5 Reanalysis at location s . We restrict the amplitude parameter $a_i(s)$ to values larger than 1 so that $a_i(s)$ acts as a multiplier on the scale of $f(s, t)$. Larger values of $a_i(s)$ correspond to increased deviations of $f(s, t)$ from its temporal mean, increasing the amplitude distance. The phase parameter $p_j(s)$ takes values in $[-1, 1]$, introducing time-warping to $f(s, t)$ which can be interpreted as changing the seasonal timing of $f(s, t)$ at location s . Positive values of $p_j(s)$ will increase the length of the summer in the northern hemisphere, and negative values will increase the length of the summer in the southern hemisphere.

The parameter fields $a_i(s)$ and $p_j(s)$ are both generated by linear functions of latitude. The amplitude parameters, $a_i(s)$, all start at a value of 1.1 at the south pole and then linearly increase to 1.2, 1.25, and 1.3 at the north pole for $i = 1, 2$, and 3, respectively. The resulting modification magnifies amplitude everywhere and intensifies with latitude. The phase parameters, $p_j(s)$, also vary linearly with latitude but start with a value of -0.2 , -0.375 , and -0.55 at the south pole and increase linearly to 0.2, 0.375, and 0.55 at the north pole for $j = 1, 2$, and 3, respectively. The resulting phase modifications create longer summer seasons the further a location is from the equator. For both $a_i(s)$ and $p_j(s)$, the most extreme amplitude and phase modifications occur for $i = j = 3$ and the least extreme modifications occur for $i = j = 1$.

We calculate the sliced amplitude and sliced phase distance between $f(s, t)$ and

each $g_{i,j}(s, t)$ following the algorithm described in Section 3.4. To understand the influence of range parameter r in the Wendland kernel function $k(u; r)$ on the distances, we repeat the calculation for four different r values in km: 210, 637, 6371, and 12742. The first range value was chosen to represent the value used in Section 5, and the remaining values were chosen to represent 5%, 10%, and 100% of the diameter of the Earth, respectively.

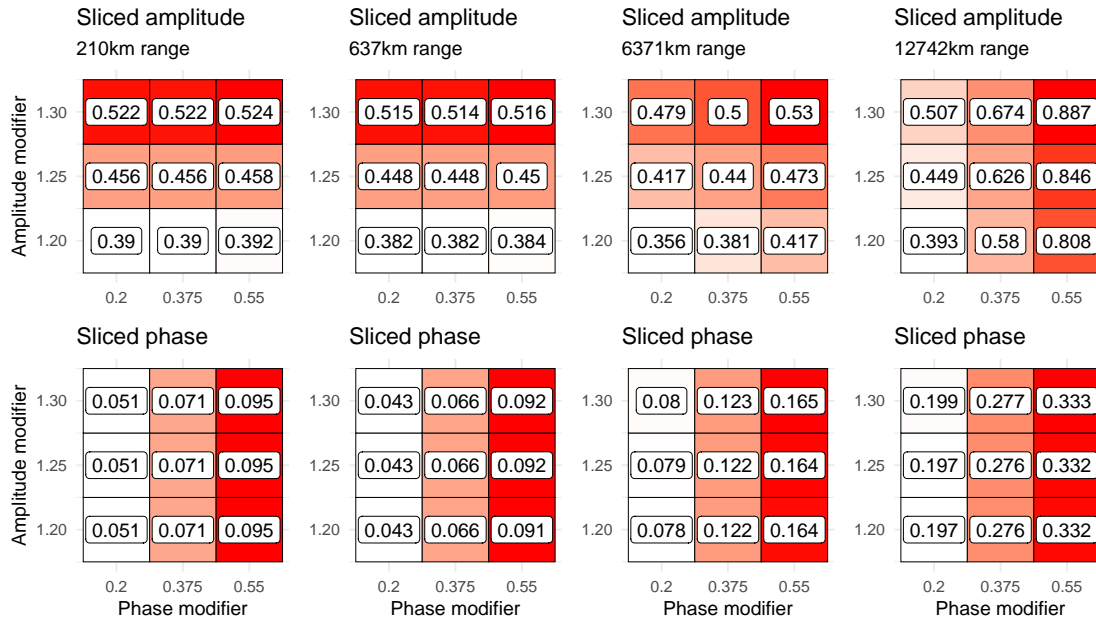


Figure 3: Sliced amplitude distance (upper) and sliced phase distance (lower) between the original ERA5 surface temperature reanalysis field, $f(s, t)$, and its modified versions, $g_{i,j}(s, t)$, at various kernel range parameter values. From the smallest to biggest, the three amplitude modifier values represent $a_1(s), a_2(s)$ and $a_3(s)$, and the three phase modifier values represent $p_1(s), p_2(s)$ and $p_3(s)$. Larger values of the amplitude and phase modifiers correspond to larger modifications made to $f(s, t)$. Color fill is unique to each individual table, with white representing the lowest value and red representing the highest.

Simulation results are reported in Figure 3. Overall, the sliced amplitude and

sliced phase distance patterns show that our method is able to separate the spatially-varying amplitude from the spatially-varying phase differences. However, the range parameter values can affect this ability. For range values of 210km and 637km, there is little to no influence of the phase modifier $p_j(s)$ on the sliced amplitude distance. Similarly, there is little to no influence of the amplitude parameter $a_i(s)$ on the sliced phase distance values. Whereas, for the range parameters of 6371km and 12742km, the sliced amplitude distances increase with $p_j(s)$, and the sliced phase distances also increase marginally with $a_i(s)$, showing evidence of entangled sliced amplitude and sliced phase distances. This is because functional data that are further away in space may have more distinct phase characteristics. When using larger range parameter values, the kernel convolution used to create the slices tends to be a cross-sectional weighted mean of misaligned functional data. Ignoring phase variability when taking functional means often destroys data structure (Tucker et al., 2013), so we recommend choosing smaller range parameter values to decrease the influence of phase variability within the kernel radius. However, the grid size of data products must be considered in the choice of range parameter. If the range parameter is chosen to be significantly smaller than the grid size of the data, the slice functions will not contain the desired level of spatial detail.

Figure 4 visualizes the amplitude and phase distances between each pair of slices of $f(s, t)$ and $g_{ij}(s, t)$ for two different simulation scenarios ($i = j = 1$ and $i = j = 3$). We see that the spatial trends in the adjusted sliced amplitude and sliced phase distances reflect the latitude trends induced by $a_i(s)$ and $p_j(s)$ as expected. Noise appears in the maps of sliced amplitude and sliced phase distance due to the discrete approximation of the phase alignment and time warping steps detailed in Section 3.4. This noise is most apparent in regions with volatile seasonal variability, such as near the equator.

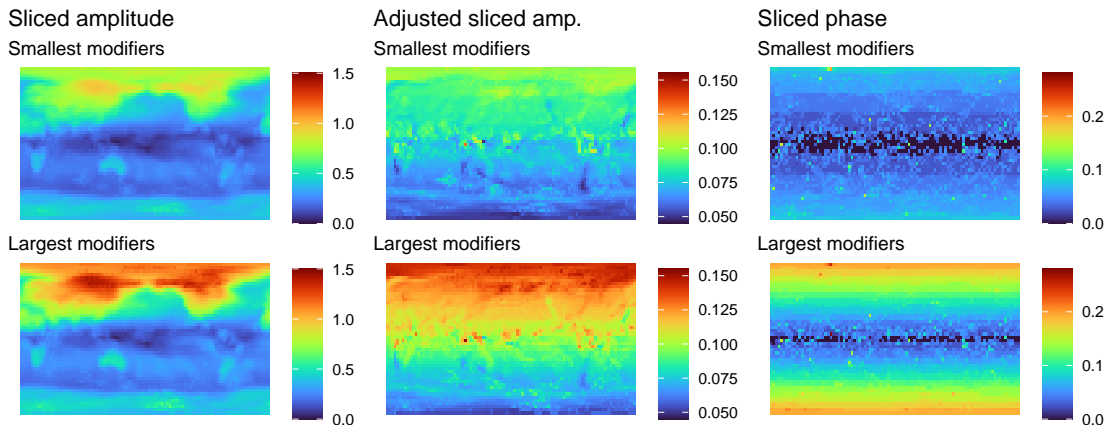


Figure 4: Map of amplitude distance (left), adjusted amplitude distance (middle), and phase distance (right) between each pair of slices of $f(s, t)$ and $g_{ij}(s, t)$ for $i = j = 1$ (upper) and $i = j = 3$ (bottom), using the kernel with $r = 637\text{km}$. The middle column shows the amplitude distance values (left) divided by $\|f(s, t)\|_2$, the L_2 norm of the time series at each location, to account for amplitude variability over space exhibited in the original ERA5 Reanalysis data.

Figure 5 shows the performance of the sliced amplitude and sliced phase distances alongside two previous methods: cross-sectional RMSE, calculated as the Euclidean norm between two spatiotemporal fields, and the Wasserstein-based method introduced in Vissio et al. (2020). Since the Wasserstein-based metric reduces spatiotemporal fields into a single univariate time series of global means, the efficient univariate Wasserstein distance calculation used in Rabin et al. (2011) is leveraged to compute exact Wasserstein distances instead of the discretization used in Vissio et al. (2020). While the sliced elastic distance metric can differentiate amplitude variability from phase variability, the RMSE and Wasserstein-based method are both unable to distinguish between sources of variability, resulting in distances that are essentially a joint reflection of both the amplitude and phase modifications.

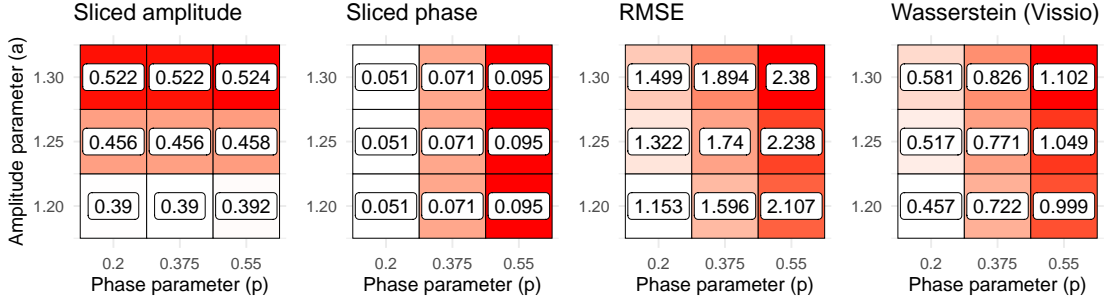


Figure 5: Sliced amplitude and sliced phase distances, Euclidean distance (RMSE), and the Wasserstein-based distance introduced in Vissio et al. (2020) between $f(s, t)$ and $g_{i,j}(s, t)$ at the kernel range parameter $r = 210\text{km}$. From the smallest to biggest, the three amplitude parameter values represent $a_1(s), a_2(s)$ and $a_3(s)$, and the three phase parameter values represent $p_1(s), p_2(s)$ and $p_3(s)$. Color fill is unique to each individual table, with white representing the lowest value and red representing the highest.

4.2 Further comparison with Wasserstein-based method

Section 4.1 compared our method with the Wasserstein-based metric from Vissio et al. (2020) when ERA5 temperatures were modified by amplitude and phase parameters linear in latitude as in (4.1). Since Vissio et al. (2020) is the method most closely related to ours, we extend the comparison between the two methods with additional simulations. We now generate $g(s, t)$ by applying less structured modifications to the original ERA5 Reanalysis field $f(s, t)$ than in (4.1). Specifically, we have:

$$g_l(s, t) = f(s, t) + k\epsilon(s) \left\{ \frac{1 + \cos(2\pi t - \pi)}{2} \right\}, \quad (4.2)$$

where $l \in \{2, 4, 6, 8, 10\}$, and $\epsilon(s)$ is an anomaly process described below. The cosine function in the brackets introduces shape and phase variability into each $g_l(s, t)$, starting at a value of 0 in January, increasing smoothly to a value of 1 in June/July, and decreasing back to 0 in December. So, there will be no difference between $g_l(s, t)$

and $f(s, t)$ in January but the full intervention from the anomaly field $\epsilon(s)$ will be realized in June/July. The parameter l magnifies the perturbation of these anomalies. Higher values of l introduce higher levels of deviation from the original ERA5 Reanalysis field.

To generate $\epsilon(s)$, we first simulate a Gaussian random process at the full 721 by 1440 resolution of the ERA5 Reanalysis field using the `fast_Gp_sim()` function from the `GpGp` R package. This R function simulates a Gaussian process using Vecchia’s approximation (Guinness et al., 2021). We choose an exponential covariance function on \mathbb{S}^2 with unit variance, zero nugget, range of 10% of the Earth’s diameter, and choose 20 nearest neighbors in the approximation. After the Gaussian field is generated, we center the field around 0 and scale the field to take values in $[-1, 1]$. A single $\epsilon(s)$ field is used in the generation of g_l for all values of l .

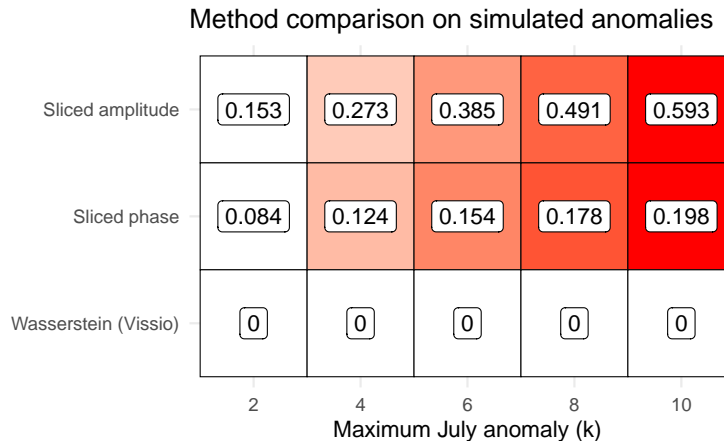


Figure 6: Sliced amplitude and sliced phase distances with a kernel range parameter of 210km compared to the Wasserstein-based method introduced in Vissio et al. (2020) between $f(s, t)$ and $g_l(s, t)$. A larger l in the x-axis indicates a larger deviation of $g_l(s, t)$ from $f(s, t)$. Color fill is unique to each individual row, with white representing the lowest value and red representing the highest value in the row. The method from Vissio et al. (2020) returns a distance of 0 for all simulations.

Sliced amplitude, sliced phase, and Wasserstein-based distances are calculated between $f(s, t)$ and each $g_l(s, t)$. For sliced amplitude and sliced phase distance, a range parameter of 210km is chosen for the Wendland kernel function $k_s(u; r)$. Figure 6 shows the results of these simulations. Sliced amplitude and sliced phase are able to recognize the increasing magnitude of the anomalies with the parameter l . However, the Wasserstein-based method by Vissio et al. (2020) has a distance of 0 for all values of l . This is because the simulated anomalies are centered around 0 resulting in no influence on the spatial mean that Vissio et al. (2020) is focused on. Although the simulated data represents an extreme situation in which anomalies are perfectly balanced, it is not unrealistic to expect discrepancies between climate fields to be centered near 0. This study illustrates the importance of capturing spatial variability in spatiotemporal fields comparison and demonstrates the ability of our sliced elastic distance in capturing spatially varying features.

5 Climate Model Validation

We first evaluate the historical reconstructive skill of individual CMIP6 climate models. We compute the sliced elastic distance between each model in CMIP6 and the ERA5 Reanalysis dataset for both temperature and precipitation fields. We then use our method to evaluate reconstructive improvements from CMIP5 to CMIP6. We similarly compute the sliced elastic distance between CMIP5 models and the ERA5 Reanalysis field and compare these distances with their CMIP6 counterparts. Lastly, we compare results from previous methods to ours in evaluating the difference between ERA5 and CMIP models and between ERA5 and the NCEP Reanalysis dataset.

For all sliced elastic distance computations, we follow the steps detailed in Section 3.4. Our choice of kernel function is the Wendland function in (3.5) with a range

parameter of 210km. The range parameter matches the size of the grid cells near the equator in the lowest-resolution CMIP model. This choice avoids the issues with larger range parameter values where sliced amplitude and sliced phase distances become entangled as demonstrated in Section 4.1.

5.1 Ranking CMIP6 models

To evaluate the reconstructive skill of CMIP6, we first create a 48-member ensemble of historical CMIP6 models runs from January 1979 through November 2005. We compute the sliced elastic distance between each model and the ERA5 Reanalysis data product observed over the same time period. Smaller sliced amplitude distances indicate that the model more closely matches the dynamics of the reanalysis field, while smaller sliced phase distance indicates closer agreement in the timing of events and seasons. Because we do not ever expect perfect agreement between models and data, we also compute the distance between NCEP Reanalysis fields and ERA5 Reanalysis fields to serve as a baseline for comparison as was done in Vissio et al. (2020).

For each climate variable, Figure 7 provides the results on a scatter plot with sliced amplitude distance on the y-axis and sliced phase distance on the x-axis. Our baseline NCEP Reanalysis fields predictably show the closest agreement with the ERA5 Reanalysis in terms of amplitude and phase. Models which share a prefix, indicating that they are from the same climate modeling center, tend to have similar values for both sliced amplitude and sliced phase distance. For both temperature and precipitation, there is evidence of a positive correlation between sliced amplitude and sliced phase distance. This implies that a model which performs well in one component (amplitude or phase) likely performs well in the other. Overall, the small distance values for NCEP and the clustering of the climate models in the same modeling group further endorse the reliability of our distance metric in evaluating climate fields.

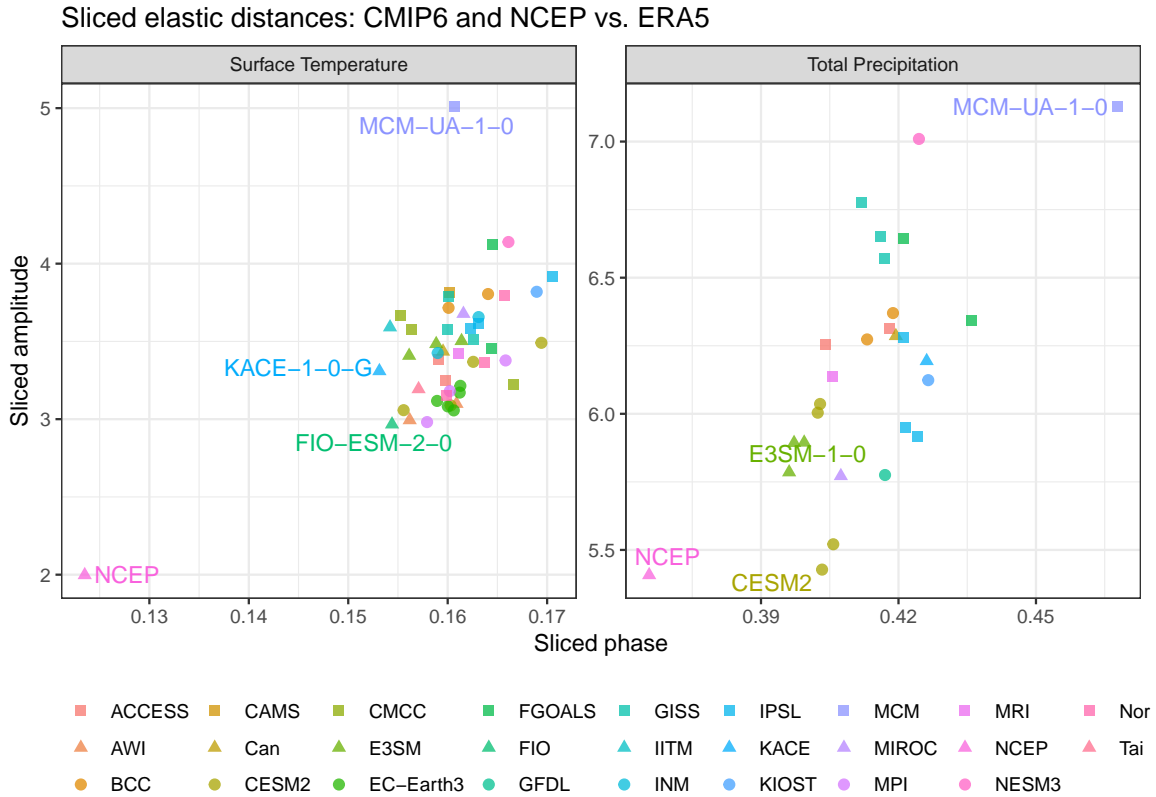


Figure 7: Sliced amplitude and sliced phase distances of CMIP6 model outputs and NCEP Reanalysis to the ERA5 Reanalysis for both average monthly (2m) surface temperature and total monthly precipitation. Values closer to 0 on each axis indicate that a model is more similar to the ERA5 Reanalysis. Models are organized by color and shape using their prefix instead of full model name in order to group models from the same climate modeling center and provide a clearer visualization. Figures 10 and 11 in Appendix C provide full tables of the results shown here.

Focusing on surface temperature, NCEP has much smaller sliced amplitude and sliced phase distances from ERA5 than all CMIP6 models. This is anticipated as the two reanalysis data, both based on observations, are expected to be closer to each other than the climate models. Among the CMIP6 models, MCM-UA-1-0 provided by the Department of Geosciences at the University of Arizona stands out as an outlier

with an abnormally large sliced amplitude distance. After some research, we found that the MCM-UA-1-0 model was developed in 1991 and designed to be extremely computationally efficient (Stouffer, 2019). The First Institute of Oceanography Earth System Model version 2.0 (FIO-ESM-2-0) has the lowest sliced amplitude distance among all CMIP6 models as well as one of the lowest values for sliced phase distance. The National Institute of Meteorological Sciences (NIMS) and Korea Meteorological Administration (KMA) team model (KACE-1-0-G) has the lowest value for sliced phase distance by a small margin. For some modeling groups, such as E3SM and GISS, there are strong similarities between each model in terms of their sliced amplitude and phase distance.

For total precipitation, the NCEP Reanalysis has a clear separation in sliced phase distance but has the lowest sliced amplitude distance by only a small margin. Again, MCM-UA-1-0 stands out as an outlier, this time in sliced phase distance. For many climate modeling centers, including E3SM, GISS, FGOALS, IPSL, CESM, and ACCESS, strong similarities are present between each model's sliced amplitude and sliced phase distance values. No single precipitation model has both the lowest sliced amplitude and sliced phase distance. The Community Earth System Models (CESM) perform best in sliced amplitude, but the Energy Exascale Earth System Models (E3SM) perform best in sliced phase, though only by a narrow margin compared to CESM. The sliced amplitude distances are spread more evenly for precipitation than for temperature, suggesting greater discrepancies in the ability of CMIP6 models to capture historical precipitation conditions. The larger sliced elastic distance values for precipitation may also imply greater challenges in modeling precipitation than temperature.

The sliced elastic distance is calculated based on local amplitude and phase distances, which can provide more detailed spatial information about the differences

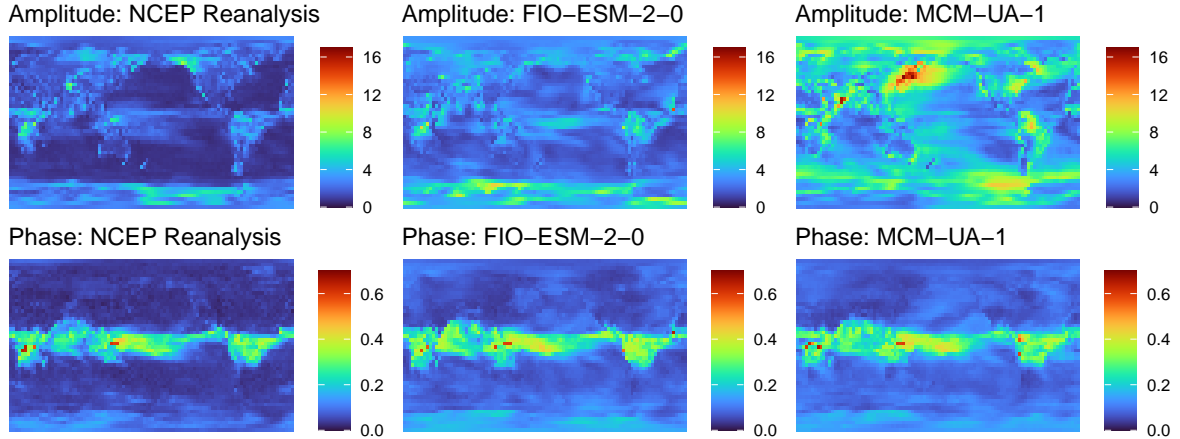


Figure 8: Maps of amplitude (upper) and phase variability (lower) for three surface temperature fields: NCEP (left), FIO-ESM-2-0 (middle), and MCM-UA-1 (right). At each location, amplitude and phase distances between the slices for each field and the ERA5 Reanalysis are recorded. Sliced amplitude and sliced phase distances are calculated as a weighted average of these amplitude and phase distances.

between two spatiotemporal fields. We pick three surface temperature fields of our interest, the NCEP Reanalysis, FIO-ESM-2-0, and MCM-UA-1-0, to show the map of these local distances compared to the ERA5 Reanalysis, see Figure 8. The FIO model seems to have a spatial pattern of amplitude distances similar to that of the NCEP Reanalysis but with higher values at almost every location. For the FIO model, notable increases in amplitude distance relative to NCEP can be seen in Antarctica, the northern regions of South America, and Greenland. Consistent with Figure 7, the MCM model shows a much higher amplitude distance over the globe, including a prominent surge in amplitude discrepancies over the east coast of the Asian continent. These hot spots for amplitude variability highlight potential issues to which climate scientists may want to pay more careful attention. For each model and NCEP, phase distances seem highest near the equator, thanks to the irregular and relatively small seasonal trend in that area. If phase variability is of particular interest in a

specific region, a follow-up study with a higher spatial resolution in that area could be performed.

5.2 Comparing CMIP5 and CMIP6

As climate models evolve and new CMIP eras are released, it is important to compare the performance of new models to previous ones to promote accuracy and innovation. Recently, many studies have been conducted to compare the new CMIP6 models to those in CMIP5. Of these, many restrict their focus to specific regions (Gusain et al., 2020; Yuanhai et al., 2020; Zamani et al., 2020; Zhu et al., 2020; Zhu and Yang, 2020; Xin et al., 2020). Others, such as Li et al. (2021), Chen et al. (2020), Fan et al. (2020) and Ukkola et al. (2020) share our global focus. Whether regional or global in focus, none of these analyses take into account the differences due to misalignment in time. Indeed, the majority of the studies used cross-sectional metrics to compare CMIP models.

We use sliced elastic distance to compare CMIP5 and CMIP6 by their similarity to the ERA5 Reanalysis. Building upon the CMIP6 analysis, we compute the sliced amplitude and sliced phase distances for each CMIP5 model against the ERA5 Reanalysis. Figure 9 provides a comparison of the CMIP5 and CMIP6 sliced elastic distance rankings.

For both climate variables, more of the CMIP6 models have lower values for the sliced amplitude distance than the CMIP5 models. This is reflected by the two median points. This shows that over the historical period, the climate dynamics represented by CMIP6 models on average are more similar to the ERA5 Reanalysis than those for the CMIP5 models. However, for sliced phase distance, the message is less clear. For surface temperature, the median sliced phase distance indicates that on average, CMIP6 performs slightly better than CMIP5. For total precipitation, the median

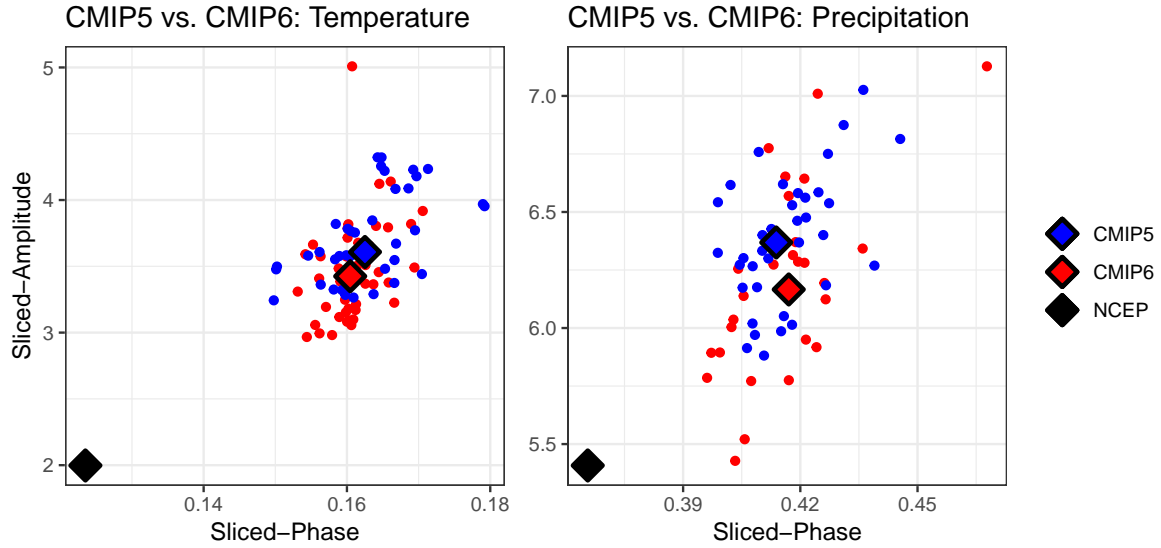


Figure 9: Sliced amplitude and sliced phase distance values from the CMIP5 (blue) and CMIP6 (red) model outputs to the ERA5 Reanalysis for both surface temperature (left) and total precipitation (right). Additional points are included on each plot for the NCEP Reanalysis, as well as median sliced amplitude and sliced phase values over all CMIP5 and CMIP6 models.

value for sliced phase distance is slightly lower for CMIP5 than for CMIP6. Given the limitations in reanalysis data products for historical precipitation (Tapiador et al., 2017) and considering that climate models are designed to provide general estimates of climate conditions rather than reproduce exact weather sequences (Roca et al., 2021), phase comparisons for precipitation may be less reliable than for temperature.

5.3 Comparing to previous methods

Appendix C provides tables of climate model rankings based on sliced amplitude distance, sliced phase distance, sliced translation distance, RMSE, and the global Wasserstein-based method by Vissio et al. (2020). Distances are calculated from the ERA5 Reanalysis field to each CMIP5 and CMIP6 model and the NCEP Reanalysis

for mean monthly (2m) surface temperature and total monthly precipitation.

As shown earlier, for both climate variables and both CMIP eras, the NCEP Reanalysis has a smaller sliced amplitude, sliced phase, and sliced translation distance than all climate model output fields. Results in Appendix C show that the RMSE metric also supports this conclusion. However, with the Wasserstein-based method, the NCEP Reanalysis ranks close to the median rank of CMIP5 and CMIP6 surface temperature models and among the worst of CMIP5 and CMIP6 total precipitation models. This is consistent with the results seen in the analysis from Vissio et al. (2020). Based on our simulation results in Section 4.2, we conjecture that this could be due to the offset of local spatial features when using a global mean projection as in Vissio et al. (2020). In all cases, the sliced amplitude distance rankings seem to have a strong positive correlation with RMSE and a weak but still positive correlation with sliced phase distance. There seems to be no obvious correlation between the rankings from the Wasserstein-based metric and the other methods.

6 Discussion

Climate model validation is critical for ensuring that climate models faithfully represent the Earth system. To this end, we developed a new metric called sliced elastic distance for quantifying model performance in a way that accounts for both spatial and temporal variability. The sliced elastic distance is a vector-valued metric that represents the amplitude, phase, and translation distance between two spatiotemporal processes. It extends the ordinary elastic distance by allowing for spatially varying warping via a kernel convolution procedure. We focus on amplitude and phase in evaluating climate models. Amplitude variability corresponds to differences in the underlying dynamics of climate models, while phase variability corresponds to errors

in the timing of seasonal transitions and weather events. Distinguishing these two components provides us with more insight into the sources of model misfit. By applying our method to evaluate CMIP5 and CMIP6 models with respect to surface temperature and total precipitation fields, we quantified how each model performs using their amplitude and phase distance to reanalysis data. We also examined the relative changes from CMIP5 to CMIP6 and identified the advancement and challenges in climate model evolution.

Our method can be computationally expensive when a large number of slices or time periods is considered. This is due to the quadratic computation time and space complexity of the dynamic programming algorithm in Tucker (2020), and is further exacerbated when a high sampling rate is employed in order to produce quality approximations of the slice SRVFs and avoid inflation of amplitude distances. The introduction of a warping window constraint was helpful in mitigating this concern, but a faster dynamic programming algorithm should be further investigated. Another limitation of our method is that the slicing process does not include a formal alignment step for the spatial domain as there is for the time domain. Incorporating spatial alignment could be especially useful for precipitation because it would allow us to identify and quantify differences in the location of precipitation events between climate models and reanalysis data.

Although our method was developed in the context of climate model validation, it can be applied to compare any two spatiotemporal processes or spatially-indexed functional data. In particular, the sliced elastic distance could be a valuable tool to introduce phase alignment into the climate model tuning process (Hourdin et al., 2017). Other possible applications include comparing spectral data from remote sensing data products, analyzing the functional measurements obtained from atomic-scale microscopy in material science, and video processing, where the considerations made

for spherical data in our method would apply directly to 360° videos.

7 Acknowledgements

This research was partially supported by the National Science Foundation through awards DGE-1922758 and DMS-2124576. We would like to thank Robert Krueger for the interesting discussions on convolution theorems and spherical harmonics.

References

- Ayugi, B., Zhihong, J., Zhu, H., Ngoma, H., Babalousmail, H., Rizwan, K., and Dike, V. (2021). Comparison of cmip6 and cmip5 models in simulating mean and extreme precipitation over east africa. *International Journal of Climatology*, 41(15):6474–6496.
- Bernal, J., Lawrence, J., Dogan, G., and Hagwood, R. (2021). On computing elastic shape distances between curves in d- dimensional space. *NIST Technical Note*, 2164.
- Bindoff, N. L., Stott, P. A., AchutaRao, K. M., Allen, M. R., Gillett, N., Gutzler, D., Hansingo, K., Hegerl, G., Hu, Y., Jain, S., et al. (2014). Detection and attribution of climate change: from global to regional.
- Briggs, W. M. and Levine, R. A. (1997). Wavelets and field forecast verification. *Monthly Weather Review*, 125(6):1329–1341.
- Chen, H., Sun, J., Lin, W., and Xu, H. (2020). Comparison of cmip6 and cmip5 models in simulating climate extremes. *Science Bulletin*, 65.
- Cressie, N., Pavlicová, M., and Santner, T. J. (2008). Detecting signals in fmri data using powerful fdr procedures. *Statistics and its interface*, 1(1):23–32.

- Dokmanic, I. and Petrinovic, D. (2009). Convolution on the n -sphere with application to pdf modeling. *IEEE transactions on signal processing*, 58(3):1157–1170.
- Driscoll, J. R. and Healy, D. M. (1994). Computing fourier transforms and convolutions on the 2-sphere. *Advances in applied mathematics*, 15(2):202–250.
- Eyring, V., Bony, S., Meehl, G. A., Senior, C. A., Stevens, B., Stouffer, R. J., and Taylor, K. E. (2016). Overview of the coupled model intercomparison project phase 6 (cmip6) experimental design and organization. *Geoscientific Model Development*, 9(5):1937–1958.
- Fan, X., Miao, C., Duan, Q., Shen, C., and Wu, Y. (2020). The performance of cmip6 versus cmip5 in simulating temperature extremes over the global land surface. *Journal of Geophysical Research: Atmospheres*, 125(18):e2020JD033031.
- Flato, G., Marotzke, J., Abiodun, B., Braconnot, P., Chou, S. C., Collins, W., Cox, P., Driouech, F., Emori, S., Eyring, V., et al. (2014). Evaluation of climate models. In *Climate change 2013: the physical science basis. Contribution of Working Group I to the Fifth Assessment Report of the Intergovernmental Panel on Climate Change*, pages 741–866. Cambridge University Press.
- Guinness, J., Katzfuss, M., and Fahmy, Y. (2021). Gpgp: fast gaussian process computation using vecchia’s approximation. *R package version 0.4. 0*.
- Gusain, A., Ghosh, S., and Karmakar, S. (2020). Added value of cmip6 over cmip5 models in simulating indian summer monsoon rainfall. *Atmospheric Research*, 232:104680.
- Harris, T., Li, B., Steiger, N. J., Smerdon, J. E., Narisetty, N., and Tucker, J. D. (2021). Evaluating proxy influence in assimilated paleoclimate reconstructions—testing the exchangeability of two ensembles of spatial processes. *Journal of the American Statistical Association*, 116(535):1100–1113.
- Hartman, E., Sukurdeep, Y., Charon, N., Klassen, E., and Bauer, M. (2021). Su-

- pervised deep learning of elastic srv distances on the shape space of curves. In *Proceedings of the IEEE/CVF conference on computer vision and pattern recognition*, pages 4425–4433.
- Heaton, M., Katzfuss, M., Berrett, C., and Nychka, D. (2014). Constructing valid spatial processes on the sphere using kernel convolutions. *Environmetrics*, 25(1):2–15.
- Hering, A. S. and Genton, M. G. (2011). Comparing spatial predictions. *Technometrics*, 53(4):414–425.
- Hersbach, H., Bell, B., Berrisford, P., Biavati, G., Horányi, A., Muñoz Sabater, J., Nicolas, J., Peubey, C., Radu, R., Rozum, I., Schepers, D., Simmons, A., Soci, C., Dee, D., and Thépaut, J.-N. (2023). Era5 monthly averaged data on single levels from 1940 to present. Accessed on 02-03-2021.
- Hersbach, H., Bell, B., Berrisford, P., Hirahara, S., Horányi, A., Muñoz-Sabater, J., Nicolas, J., Peubey, C., Radu, R., Schepers, D., et al. (2020). The era5 global reanalysis. *Quarterly Journal of the Royal Meteorological Society*, 146(730):1999–2049.
- Horváth, L., Kokoszka, P., and Reeder, R. (2013). Estimation of the mean of functional time series and a two-sample problem. *Journal of the Royal Statistical Society: Series B (Statistical Methodology)*, 75(1):103–122.
- Hourdin, F., Mauritsen, T., Gettelman, A., Golaz, J.-C., Balaji, V., Duan, Q., Folini, D., Ji, D., Klocke, D., Qian, Y., et al. (2017). The art and science of climate model tuning. *Bulletin of the American Meteorological Society*, 98(3):589–602.
- Hubbert, S. and Jäger, J. (2023). Generalised wendland functions for the sphere. *Advances in Computational Mathematics*, 49(1):3.
- Jachymski, J. and Klima, J. (2016). Around perov’s fixed point theorem for mappings on generalized metric spaces. *Fixed Point Theory*, 17(2):367–380.

- Joshi, S. H., Klassen, E., Srivastava, A., and Jermyn, I. (2007). A novel representation for riemannian analysis of elastic curves in \mathbb{R}^n . In *2007 IEEE Conference on Computer Vision and Pattern Recognition*, pages 1–7. IEEE.
- Karim, R., Tan, G., Ayugi, B., Babaousmail, H., and Liu, F. (2020). Evaluation of historical cmip6 model simulations of seasonal mean temperature over pakistan during 1970–2014. *Atmosphere*, 11(9):1005.
- Kent, J. T. (1982). The fisher-bingham distribution on the sphere. *Journal of the Royal Statistical Society: Series B (Methodological)*, 44(1):71–80.
- Li, B. and Smerdon, J. E. (2012). Defining spatial comparison metrics for evaluation of paleoclimatic field reconstructions of the common era. *Environmetrics*, 23(5):394–406.
- Li, B., Zhang, X., and Smerdon, J. E. (2016). Comparison between spatio-temporal random processes and application to climate model data. *Environmetrics*, 27(5):267–279.
- Li, J., Huo, R., Chen, H., Zhao, Y., and Zhao, T. (2021). Comparative assessment and future prediction using cmip6 and cmip5 for annual precipitation and extreme precipitation simulation. *Frontiers in Earth Science*, 9.
- Lund, R. and Li, B. (2009). Revisiting climate region definitions via clustering. *Journal of Climate*, 22(7):1787–1800.
- Manole, T., Balakrishnan, S., and Wasserman, L. (2022). Minimax confidence intervals for the sliced wasserstein distance. *Electronic Journal of Statistics*, 16(1).
- Nychka, D., Bandyopadhyay, S., Hammerling, D., Lindgren, F., and Sain, S. (2015). A multiresolution gaussian process model for the analysis of large spatial datasets. *Journal of Computational and Graphical Statistics*, 24(2):579–599.
- Raäisaänen, J. (2007). How reliable are climate models? *Tellus A: Dynamic Meteorology and Oceanography*, 59(1):2–29.

- Rabin, J., Peyré, G., Delon, J., and Bernot, M. (2011). Wasserstein barycenter and its application to texture mixing. In *International Conference on Scale Space and Variational Methods in Computer Vision*, pages 435–446. Springer.
- Ramsay, J. O. and Silverman, B. W. (2005). *Fitting differential equations to functional data: Principal differential analysis*. Springer.
- Rao, S. S. (2015). On vector valued metric spaces. *Palestine Journal of Mathematics*, 4(2):416–418.
- Roca, R., Haddad, Z. S., Akimoto, F. F., Alexander, L., Behrangi, A., Huffman, G., Kato, S., Kidd, C., Kirstetter, P.-E., Kubota, T., et al. (2021). The joint ipwg/gewex precipitation assessment.
- Rood, R. B. (2019). *Validation of Climate Models: An Essential Practice*, pages 737–762. Springer International Publishing, Cham.
- Sastry, K., Naidu, G., Bekeshie, T., and Rahamatulla, M. (2012). A common fixed point theorem for four self maps in complex valued and vector valued metric spaces. *Int. J. Math. Arc*, 3:2680–2685.
- Shen, X., Huang, H.-C., and Cressie, N. (2002). Nonparametric hypothesis testing for a spatial signal. *Journal of the American Statistical Association*, 97(460):1122–1140.
- Snell, S. E., Gopal, S., and Kaufmann, R. K. (2000). Spatial interpolation of surface air temperatures using artificial neural networks: Evaluating their use for down-scaling gcms. *Journal of Climate*, 13(5):886–895.
- Srivastava, A. and Klassen, E. P. (2016). *Functional and shape data analysis*, volume 1. Springer.
- Staicu, A.-M., Li, Y., Crainiceanu, C. M., and Ruppert, D. (2014). Likelihood ratio tests for dependent data with applications to longitudinal and functional data analysis. *Scandinavian Journal of Statistics*, 41(4):932–949.

- Stouffer, R. (2019). U of arizona mcm-ua-1-0 model output prepared for cmip6 cmip.
- Tapiador, F., Navarro, A., Levizzani, V., García-Ortega, E., Huffman, G., Kidd, C., Kucera, P., Kummerow, C., Masunaga, H., Petersen, W., et al. (2017). Global precipitation measurements for validating climate models. *Atmospheric Research*, 197:1–20.
- Tucker, J. D. (2020). *fdasrvf: Elastic Functional Data Analysis*. R package version 1.9.3.
- Tucker, J. D., Martinez, M. T., and Laborde, J. M. (2022). Dimensionality reduction using elastic measures. *arXiv preprint arXiv:2209.04933*.
- Tucker, J. D., Wu, W., and Srivastava, A. (2013). Generative models for functional data using phase and amplitude separation. *Computational Statistics & Data Analysis*, 61:50–66.
- Ukkola, A. M., De Kauwe, M. G., Roderick, M. L., Abramowitz, G., and Pitman, A. J. (2020). Robust future changes in meteorological drought in cmip6 projections despite uncertainty in precipitation. *Geophysical Research Letters*, 47(11):e2020GL087820.
- Vissio, G., Lembo, V., Lucarini, V., and Ghil, M. (2020). Evaluating the performance of climate models based on wasserstein distance. *Geophysical Research Letters*, 47(21):e2020GL089385. e2020GL089385 10.1029/2020GL089385.
- Wang, W., Anderson, B. T., Entekhabi, D., Huang, D., Su, Y., Kaufmann, R. K., and Myneni, R. B. (2007). Intraseasonal interactions between temperature and vegetation over the boreal forests. *Earth Interactions*, 11(18):1–30.
- Washington, W. M. and Parkinson, C. (2005). *Introduction to three-dimensional climate modeling*. University science books.
- Wendland, H. (1998). Error estimates for interpolation by compactly supported radial basis functions of minimal degree. *Journal of approximation theory*, 93(2):258–272.

- Xin, X., Wu, T., Zhang, J., Yao, J., and Fang, Y. (2020). Comparison of cmip6 and cmip5 simulations of precipitation in china and the east asian summer monsoon. *International Journal of Climatology*, 40(15):6423–6440.
- Yuanhai, F. U., Lin, Z., and Guo, D. (2020). Improvement of the simulation of the summer east asian westerly jet from cmip5 to cmip6. *Atmospheric and Oceanic Science Letters*, 13(6):550–558.
- Zamani, Y., Hashemi Monfared, S. A., Hamidianpour, M., et al. (2020). A comparison of cmip6 and cmip5 projections for precipitation to observational data: the case of northeastern iran. *Theoretical and Applied Climatology*, 142(3):1613–1623.
- Zhang, J.-T. and Chen, J. (2007). Statistical inferences for functional data.
- Zhang, X. and Shao, X. (2015). Two sample inference for the second-order property of temporally dependent functional data.
- Zhao, S., He, W., Dong, T., Zhou, J., Xie, X., Mei, Y., Wan, S., and Jiang, Y. (2021). Evaluation of the performance of cmip5 models to simulate land surface air temperature based on long-range correlation. *Frontiers in Environmental Science*, page 6.
- Zhu, H., Jiang, Z., Li, J., Li, W., Sun, C., and Li, L. (2020). Does cmip6 inspire more confidence in simulating climate extremes over china? *Advances in Atmospheric Sciences*, 37(10):1119–1132.
- Zhu, Y.-Y. and Yang, S. (2020). Evaluation of cmip6 for historical temperature and precipitation over the tibetan plateau and its comparison with cmip5. *Advances in Climate Change Research*, 11(3):239–251.

A Data description

Table 1: List of obtained climate model outputs and reanalysis data products.

(a) Reanalysis Data

Reanalysis	Date Range	Spatial Res.
ERA5	1979-present	1440 × 721
NCEP	1979-present	192 × 94

(c) CMIP6 Models

Model	Date Range	Spatial Res.
ACCESS-CM2	1850-2014	192 × 144
ACCESS-ESM1-5	1850-2014	192 × 145
AWI-CM-1-1-MR	1979-2005	384 × 192
AWI-ESM-1-1-LR	1979-2005	192 × 96
BCC-CSM2-MR	1850-2014	320 × 160
BCC-ESM1	1850-2014	128 × 64
CAMS-CSM1-0	1850-2014	320 × 160
CESM2	1850-2014	288 × 192
CESM2-FV2	1950-2014	144 × 96
CESM2-WACCM	1850-2014	288 × 192
CESM2-WACCM-FV2	1950-2014	144 × 96
CMCC-CM2-HR4	1850-2014	288 × 192
CMCC-CM2-SR5	1850-2014	288 × 192
CMCC-ESM2	1850-2014	288 × 192
CanESM5	1850-2014	128 × 64
E3SM-1-0	1975-2014	360 × 180
E3SM-1-1	1970-2009	360 × 180
E3SM-1-1-ECA	1970-2009	360 × 180
EC-Earth3	1979-2005	512 × 256
EC-Earth3-AerChem	1979-2005	512 × 256
EC-Earth3-CC	1979-2005	512 × 256
EC-Earth3-Veg	1979-2005	512 × 256
EC-Earth3-Veg-LR	1979-2005	320 × 160
FGOALS-f3-L	1850-2014	288 × 180
FGOALS-g3	1970-2009	180 × 80
FIO-ESM-2-0	1850-2014	288 × 192
GISS-E2-1-G	1951-2014	144 × 90
GISS-E2-1-H	1951-2014	144 × 90
GISS-E2-2-H	1976-2014	144 × 90
IITM-ESM	1970-2009	192 × 94
INM-CM4-8	1950-2014	180 × 120
INM-CM5-0	1950-2014	180 × 120
IPSL-CM5A2-INCA	1850-2014	96 × 96
IPSL-CM6A-LR	1850-2014	144 × 143
IPSL-CM6A-LR-INCA	1850-2014	144 × 143
KACE-1-0-G	1850-2014	192 × 144
KIOST-ESM	1850-2014	192 × 96
MCM-UA-1-0	1850-2014	96 × 80
MIROC6	1950-2014	256 × 128
MPI-ESM-1-2-HAM	1970-2009	192 × 96
MPI-ESM1-2-HR	1975-2009	384 × 192
MPI-ESM1-2-LR	1970-2009	192 × 96
MRI-ESM2-0	1850-2014	320 × 160
NESM3	1850-2014	192 × 96
NorCPM1	1850-2014	144 × 96
NorESM2-LM	1970-2009	144 × 96
NorESM2-MM	1970-2009	288 × 192
TaiESM1	1850-2014	288 × 192

(b) CMIP5 Models

Model	Date Range	Spatial Res.
ACCESS1-0	1850-2005	192 × 145
ACCESS1-3	1850-2005	192 × 145
CanCM4	1961-2005	128 × 64
CanESM2	1850-2005	128 × 64
CMCC-CESM	1975-2005	96 × 48
CMCC-CM	1970-2005	480 × 240
CMCC-CMS	1970-2005	192 × 96
CNRM-CM5	1950-2005	256 × 128
CNRM-CM5-2	1950-2005	256 × 128
CSIRO-Mk3-6-0	1850-2005	192 × 96
FGOALS-s2	1850-2005	128 × 108
GFDL-CM2p1	1976-2005	144 × 90
GFDL-CM3	1975-2005	144 × 90
GFDL-ESM2G	1976-2005	144 × 90
GFDL-ESM2M	1976-2005	144 × 90
GISS-E2-H	1951-2005	144 × 90
GISS-E2-H-CC	1951-2010	144 × 90
GISS-E2-R	1976-2005	144 × 90
GISS-E2-R-CC	1976-2010	144 × 90
HadCM3	1959-2005	96 × 73
HadGEM2-AO	1860-2005	192 × 145
HadGEM2-CC	1959-2005	192 × 145
HadGEM2-ES	1959-2005	192 × 145
inmcm4	1850-2005	180 × 120
IPSL-CM5A-LR	1850-2005	96 × 96
IPSL-CM5A-MR	1850-2005	144 × 143
IPSL-CM5B-LR	1850-2005	96 × 96
MIROC-ESM	1850-2005	128 × 64
MIROC-ESM-CHEM	1850-2005	128 × 64
MIROC4h	1971-2005	640 × 320
MIROC5	1850-2012	256 × 128
MPI-ESM-LR	1850-2005	192 × 96
MPI-ESM-MR	1850-2005	192 × 96
MPI-ESM-P	1850-2005	192 × 96
MRI-CGCM3	1850-2005	320 × 160
MRI-ESM1	1851-2005	320 × 160
NorESM1-M	1850-2005	144 × 96
NorESM1-ME	1850-2005	144 × 96

B Proof of Theorem 3.2

Lemma 3.1. $D_E(f, g)$ is a vector-valued metric on $\mathcal{F}_{\mathcal{T}}$.

Proof. Proposition 2.1 in (Jachymski and Klima, 2016) provides a clear structure for our proof. First, we show that amplitude, phase, and translation distance are each a pseudometric on $\mathcal{F}_{\mathcal{T}}$. Then, we finish the proof by showing the final property: for any $f, g \in \mathcal{F}_{\mathcal{T}}$, $f \neq g \Rightarrow D_A(f, g) > 0$, $D_P(f, g) > 0$, or $D_T(f, g) > 0$.

Section 4.10.1 in (Srivastava and Klassen, 2016) shows that amplitude distance is a proper metric on the quotient space \mathbb{L}_2/Γ . Since for all functions $f, g \in \mathcal{F}_{\mathcal{T}}$, there exist unique orbits $[q_f], [q_g] \in \mathbb{L}_2/\Gamma$, the Identity, Symmetry, and Triangle Inequality properties hold trivially on $\mathcal{F}_{\mathcal{T}}$ as well.

Section 4.10.2 in (Srivastava and Klassen, 2016) shows that for two functions $f, g \in \mathcal{F}_{\mathcal{T}}$, phase distance satisfies the Identity, Symmetry, and Triangle Inequality properties on $\mathcal{F}_{\mathcal{T}}$. So, phase distance is a pseudometric on $\mathcal{F}_{\mathcal{T}}$.

For translation distance, let $f, g, h \in \mathcal{F}_{\mathcal{T}}$. Note $f(0), g(0), h(0) \in \mathbb{R}$. Then,

1. $D_T(f, f) = |f(0) - f(0)| = 0$
2. $D_T(f, g) = |f(0) - g(0)| = |g(0) - f(0)| = D_T(g, f)$
3. $D_T(f, h) = |f(0) - h(0)| \leq |f(0) - g(0)| + |g(0) - h(0)| = D_T(f, g) + D_T(g, h)$.

Therefore, translation distance is a pseudometric on $\mathcal{F}_{\mathcal{T}}$.

It remains to show that for all $f, g \in \mathcal{F}_{\mathcal{T}}$, $f \neq g \Rightarrow D_A(f, g) > 0$, $D_P(f, g) > 0$, or $D_T(f, g) > 0$. We proceed by proving the contrapositive: for all $f, g \in \mathcal{F}_{\mathcal{T}}$, if $D_A(f, g) = D_P(f, g) = D_T(f, g) = 0$ then $f = g$. Let $f, g \in \mathcal{F}_{\mathcal{T}}$ with $D_A(f, g) = D_P(f, g) = D_T(f, g) = 0$. Denote the relative phase of f with respect to g as (γ_f^*, γ_g^*) .

$D_P(f, g) = 0 \Rightarrow \gamma_f^* = \gamma_g^*$. So,

$$0 = D_A(f, g) \tag{B.1}$$

$$= \inf_{\gamma_f, \gamma_g \in \bar{\Gamma}_I} \|(q_f, \gamma_f) - (q_g, \gamma_g)\| \tag{B.2}$$

$$= \|(q_f, \gamma_f^*) - (q_g, \gamma_g^*)\| \tag{B.3}$$

$$= \|(q_f, \gamma_f^*) - (q_g, \gamma_f^*)\| \tag{B.4}$$

$$= \|q_f - q_g\|. \tag{B.5}$$

The third line follows by the definition of relative phase. The last line follows by Lemma 4.2 in (Srivastava and Klassen, 2016).

It follows by property of the Euclidean norm that $q_f = q_g$. In addition, $D_T(f, g) = 0 \Rightarrow f(0) = g(0)$. So, we have $f(0) = g(0)$ and $q_f = q_g$. By the absolute continuity of f and g , it follows that $f = g$. So, for all $f, g \in \mathcal{F}_{\mathcal{T}}$, $D_A(f, g) = D_P(f, g) = D_T(f, g) = 0 \Rightarrow f = g$.

We have shown that the elastic distance $D_E(f, g)$ is a family of pseudometrics on $\mathcal{F}_{\mathcal{T}}$ that jointly satisfies the positivity property on $\mathcal{F}_{\mathcal{T}}$. So, by Proposition 2.1 in (Jachymski and Klima, 2016), it follows that D_E is a vector-valued metric on $\mathcal{F}_{\mathcal{T}}$. \square

Lemma B.1. *If $f \in \mathcal{F}_{\mathcal{S} \times \mathcal{T}}$, then the slice $f_s(t)$ as defined in Definition 3.1 is an element of $\mathcal{F}_{\mathcal{T}}$ for all $s \in \mathcal{S}$.*

Proof. Let $f \in \mathcal{F}_{\mathcal{S} \times \mathcal{T}}$, $s^* \in \mathcal{S}$, and $r > 0$. Suppose for contradiction that $f_{s^*}(t) \notin \mathcal{F}_{\mathcal{T}}$. Then, $f_{s^*}(t)$ is not absolutely continuous, so there exists some $\epsilon^* > 0$ such that for all $\delta > 0$, there exists a finite sequence of M sub-intervals $(a_m, b_m) \in [0, 1]$, $m = 1, \dots, M$, with $\sum_{m=1}^M (b_m - a_m) < \delta$ and $\sum_{m=1}^M |f_{s^*}(a_m) - f_{s^*}(b_m)| \geq \epsilon^*$.

Let $m_{max} = \arg \max_{m \in \{1, \dots, M\}} |f_{s^*}(a_m) - f_{s^*}(b_m)|$. It follows that $|f_{s^*}(a_{m_{max}}) - f_{s^*}(b_{m_{max}})| \geq \epsilon^*/M$. For clarity, denote $t_1 = a_{m_{max}}$ and $t_2 = b_{m_{max}}$. Note that $t_2 - t_1 < \delta$. We have:

$$\epsilon^*/M \leq |f_{s^*}(t_1) - f_{s^*}(t_2)| \quad (\text{B.6})$$

$$= \left| \int_{\mathcal{S}} f(s, t_1) k_{s^*}^r(s) ds - \int_{\mathcal{S}} f(s, t_2) k_{s^*}^r(s) ds \right| \quad (\text{B.7})$$

$$= \left| \int_{\mathcal{S}} \{f(s, t_1) - f(s, t_2)\} k_{s^*}^r(s) ds \right| \quad (\text{B.8})$$

$$\leq \left[\int_{\mathcal{S}} \{f(s, t_1) - f(s, t_2)\}^2 ds \right]^{1/2} \left(\int_{\mathcal{S}} k_{s^*}^r(s)^2 ds \right)^{1/2}, \quad (\text{B.9})$$

where the last line follows by the Cauchy-Schwarz Inequality. This implies:

$$\frac{(\epsilon^*/M)^2}{\int_{\mathcal{S}} k_{s^*}^r(s)^2 ds} \leq \int_{\mathcal{S}} \{f(s, t_1) - f(s, t_2)\}^2 ds \quad (\text{B.10})$$

$$\leq \max_{s \in \mathcal{S}} \{f(s, t_1) - f(s, t_2)\}^2. \quad (\text{B.11})$$

Now, taking the square root of each side, we get:

$$\frac{\epsilon^*/M}{\left\{ \int_{\mathcal{S}} k_{s^*}^r(s)^2 ds \right\}^{1/2}} \leq \max_{s \in \mathcal{S}} |f(s, t_1) - f(s, t_2)|. \quad (\text{B.12})$$

Denote the quantity on the left side of the above inequality as:

$$\epsilon = \frac{\epsilon^*/M}{\left\{ \int_{\mathcal{S}^2} k_{s^*}^r(s)^2 ds \right\}^{1/2}}. \quad (\text{B.13})$$

Since $k_{s^*}^r(s) \geq 0$ for all $s, s^* \in \mathcal{S}$, $r > 0$ implies that $\int_{\mathcal{S}} k_{s^*}^r(s)^2 ds > 0$. So, $\epsilon > 0$. Let $s' = \arg \max_{s \in \mathcal{S}} |f(s, t_2) - f(s, t_1)|$. Now, we have found $\epsilon > 0$ such that for all $\delta > 0$, there exists a sub-interval $(t_1, t_2) \subset [0, 1]$ with $t_2 - t_1 < \delta$ and:

$$|f(s', t_2) - f(s', t_1)| \geq \epsilon. \quad (\text{B.14})$$

We have found a location $s' \in \mathcal{S}$ such that $f(s', t)$ is not an absolutely continuous function of time, so we have a contradiction of the assumption that $f \in \mathcal{F}_{\mathcal{S} \times \mathcal{T}}$. Our proof by contradiction is complete, therefore $f_s(t) \in \mathcal{F}_{\mathcal{T}}$ for all $s \in \mathcal{S}$ and $r > 0$. \square

Lemma B.2 (Slicing Extends Pseudometrics). *If D is a pseudometric on \mathcal{F} then D_S , the sliced version of D , is a pseudometric on $\mathcal{F}_{\mathcal{S} \times \mathcal{T}}$.*

Proof. Let D be a pseudometric on $\mathcal{F}_{\mathcal{T}}$. Let D_S be the sliced distance function corresponding to D following the process in Theorem 3.2. We begin by proving the identity property. Let $f(s, t) \in \mathcal{F}_{S \times \mathcal{T}}$. Then,

$$D_S(f(s, t), f(s, t)) = \left\{ \int_{S^2} D(f_s(t), f_s(t))^2 ds \right\}^{1/2} \quad (\text{B.15})$$

$$= \left\{ \int_{S^2} 0^2 ds \right\}^{1/2} \quad (\text{B.16})$$

$$= 0. \quad (\text{B.17})$$

The second line holds by the identity property of D . Next, we show the symmetry property. Let $f(s, t), g(s, t) \in \mathcal{F}_{S \times \mathcal{T}}$. Then,

$$D_S(f(s, t), g(s, t)) = \left\{ \int_{S^2} D(f_s(t), g_s(t))^2 ds \right\}^{1/2} \quad (\text{B.18})$$

$$= \left\{ \int_{S^2} D(g_s(t), f_s(t))^2 ds \right\}^{1/2} \quad (\text{B.19})$$

$$= D_S(g(s, t), f(s, t)) \quad (\text{B.20})$$

The second line holds by the symmetry property of D . Finally, we show the triangle inequality property. Let $f(s, t), g(s, t), h(s, t) \in \mathcal{F}_{S \times \mathcal{T}}$. Then,

$$D_S(f(s, t), h(s, t)) = \left\{ \int_{S^2} D(f_s(t), h_s(t))^2 ds \right\}^{1/2} \quad (\text{B.21})$$

$$\leq \left[\int_{S^2} \left\{ D(f_s(t), g_s(t)) + D(g_s(t), h_s(t)) \right\}^2 ds \right]^{1/2} \quad (\text{B.22})$$

$$\leq \left\{ \int_{S^2} D(f_s(t), g_s(t))^2 ds \right\}^{1/2} + \left\{ \int_{S^2} D(g_s(t), h_s(t))^2 ds \right\}^{1/2} \quad (\text{B.23})$$

$$= D_S(f(s, t), g(s, t)) + D_S(g(s, t), h(s, t)) \quad (\text{B.24})$$

The second line holds by the triangle inequality property of D on $\mathcal{F}_{\mathcal{T}}$. The third line holds by the Minkowski Inequality.

Finally, we have that for a pseudometric D on $\mathcal{F}_{\mathcal{T}}$, the sliced version of D , D_S , satisfies all three properties of a pseudometric on $\mathcal{F}_{\mathcal{S} \times \mathcal{T}}$. Therefore, if D is a pseudometric on $\mathcal{F}_{\mathcal{T}}$, then D_S is a pseudometric on $\mathcal{F}_{\mathcal{S} \times \mathcal{T}}$. \square

Using the previous lemmas along with results from (Driscoll and Healy, 1994), we can prove the previously stated Theorem 3.2.

Theorem 3.2. *If $D = [D_1, \dots, D_m]^T$ is a vector-valued metric on $\mathcal{F}_{\mathcal{T}}$, and $f_s(t)$ and $g_s(t)$ are respectively the slice functions of $f(u, t) \in \mathcal{F}_{\mathcal{S} \times \mathcal{T}}$ and $g(u, t) \in \mathcal{F}_{\mathcal{S} \times \mathcal{T}}$ using a spatially continuous kernel $k(u; \theta)$ with an positive spectral density on \mathcal{S} as defined in (3.3), then the vector-valued function $D_S = [D_{S1}, \dots, D_{Sm}]^T$ with each component defined as*

$$D_{Si}(f, g) = \left\{ \int_{\mathcal{S}} D_i(f_s, g_s)^2 ds \right\}^{1/2}, \quad i = 1, \dots, m,$$

is a vector-valued metric on $\mathcal{F}_{\mathcal{S} \times \mathcal{T}}$.

Proof. Let D be a vector-valued metric on $\mathcal{F}_{\mathcal{T}}$. For each $i \in \{1, \dots, m\}$, let D_{Si} be the sliced version of D_i using kernel $k(u; \theta)$. By Lemma B.2, $D_S = (D_{S1}, \dots, D_{Sm})$ is a family of pseudometrics on $\mathcal{F}_{\mathcal{S} \times \mathcal{T}}$. To show D_S is a vector-valued metric on $\mathcal{F}_{\mathcal{S} \times \mathcal{T}}$, it suffices to show that for any $f, g \in \mathcal{F}_{\mathcal{S} \times \mathcal{T}}$, if $f \neq g$ then $D_{Si}(f, g) > 0$ for some $i \in \{1, \dots, m\}$. We proceed by proving the contrapositive: for all $f, g \in \mathcal{F}_{\mathcal{S} \times \mathcal{T}}$, if $D_S(f, g) = 0_m$ then $f = g$.

Let $f, g \in \mathcal{F}_{\mathcal{S} \times \mathcal{T}}$ with $D_S(f, g) = 0_m$. Then $0 = \int_{\mathcal{S}} D_{Si}(f_s, g_s) ds$ for all $i \in \{1, \dots, m\}$. So, for all $i \in \{1, \dots, m\}$, $D_{Si}(f_s, g_s) = 0$ for almost every $s \in \mathcal{S}$. By property of vector-valued metrics, this implies that $f_s(t) = g_s(t)$ for almost every $s \in \mathcal{S}$. Let $h(s, t) = f(s, t) - g(s, t)$. Note that $h_s(t) = \int_{\mathcal{S}} \{f(u, t) - g(u, t)\} k_s(u; \theta) du = f_s(t) - g_s(t)$. So, for all $t \in \mathcal{T}$, $h_s(t) = 0$ for almost every $s \in \mathcal{S}$.

Now, fix $t \in \mathcal{T}$ and define the spatial convolution of h with k at time t as $c_{h,t}(s) = \int_{\mathcal{S}} h(u, t) k_s(u; \theta) du$. This convolution is a function of space only, serving as the spatial

version of the previously defined slice functions, which are functions of time only. Note that $c_{h,t}(s)$ is equal to 0 for almost every $s \in \mathcal{S}$ because $h_s(t) = 0$ for almost every $s \in \mathcal{S}$. Additionally, since $c_{h,t}(s)$ is defined as a convolution of continuous functions on \mathcal{S} , it is itself a continuous function on \mathcal{S} . It follows by property of continuity that $c_h(s, t) = 0$ for all $s \in \mathcal{S}$.

Using the spherical harmonics representation of $c_{h,t}(s)$ (Driscoll and Healy, 1994), we can represent $c_{h,t}(s)$ as

$$c_{h,t}(s) = \sum_{l \geq 0} \sum_{|m| \leq l} \widetilde{c}_{h,t}(l, m) Y_l^m(s). \quad (\text{B.25})$$

Where $Y_l^m(s)$ are the spherical harmonics bases and $\widetilde{c}_{h,t}(l, m)$ are the spherical harmonics coefficients for $c_{h,t}(s)$. Since the bases $Y_l^m(s)$ are orthonormal and $c_{h,t}(s) = 0$, we have that $\widetilde{c}_{h,t}(l, m) = 0$ for all l and m .

Since $c_h(s, t) = \int_{\mathcal{S}} h(u, t) k_s(u; \theta) du$ is a convolution of functions on \mathcal{S} , where \mathcal{S} was previously defined to be the 2-dimensional unit sphere, using Theorem 1 in (Driscoll and Healy, 1994) we can write the spherical harmonics coefficients $\widetilde{c}_{h,t}(l, m)$ in terms of the spherical harmonics coefficients for $h(u, t)$ and $k_s(u; \theta)$, denoted respectively as $\widetilde{h}^t(l, m)$ and $\widetilde{k}(l, m)$:

$$\widetilde{c}_{h,t}(l, m) = \alpha(l) \widetilde{h}^t(l, m) \widetilde{k}(l, 0), \quad (\text{B.26})$$

where $\alpha(l) = 2\pi \sqrt{\frac{4\pi}{2l+1}}$. Clearly $\alpha(l) > 0$ for all $l \geq 0$. By our assumption that $k(u; \theta)$ has positive spectral density on \mathcal{S} , we know that $\widetilde{k}(l, 0) > 0$ for all $l \geq 0$. Therefore, since $\widetilde{c}_{h,t}(l, m) = 0$, we must have $\widetilde{h}^t(l, m) = 0$ for all l and m . Using the spherical harmonics representation for $h(s, t)$, we can see:

$$h(s, t) = \sum_{l \geq 0} \sum_{|m| \leq l} \widetilde{h}^t(l, m) Y_l^m(s) \quad (\text{B.27})$$

$$= \sum_{l \geq 0} \sum_{|m| \leq l} 0 * Y_l^m(s) \quad (\text{B.28})$$

$$= 0. \quad (\text{B.29})$$

So, $h(s, t) = 0$ for all $s \in \mathcal{S}$. Since t was fixed arbitrarily, we also have that $h(s, t) = 0$ for all $t \in \mathcal{T}$. Therefore, $0 = h(s, t) = f(s, t) - g(s, t)$, implying that $f = g$.

We have shown that for all $f, g \in \mathcal{F}_{\mathcal{S} \times \mathcal{T}}$, if $D_S(f, g) = 0_m$, then $f = g$. Our proof by contrapositive is complete, therefore for all $f, g \in \mathcal{F}_{\mathcal{S} \times \mathcal{T}}$, if $f \neq g$, then $D_{S_i}(f, g) > 0$ for some $i \in \{1, \dots, n\}$. So, for any vector-valued metric D on \mathcal{F} , D_S is a family of pseudometrics that jointly satisfies the positivity property on $\mathcal{F}_{\mathcal{S} \times \mathcal{T}}$. Therefore, by Proposition 2.1 in (Jachymski and Klima, 2016), if D is a vector-valued metric on $\mathcal{F}_{\mathcal{T}}$ and $k(u; \theta)$ is a continuous spatial kernel with positive spectral density on \mathcal{S} , then D_S , the sliced version of D defined using $k(u; \theta)$, is a vector-valued metric on $\mathcal{F}_{\mathcal{S} \times \mathcal{T}}$. □

C Tables of Results

Metric comparison: CMIP6 surface temperature

	Sliced Amplitude	Sliced Phase	Sliced Translation	Vissio et al.	RMSE
NCEP Reanalysis -	1.998	0.123	1.814	0.459	2.035
FIO-ESM-2-0	2.967	0.154	2.866	0.129	2.610
MPI-ESM1-2-HR	2.981	0.158	2.183	0.476	2.517
AWI-CM-1-1-MR	2.994	0.156	2.544	0.393	2.481
EC-Earth3-AerChem	3.056	0.161	2.483	0.285	2.898
CESM2	3.058	0.156	2.869	0.358	2.550
EC-Earth3-Veg	3.082	0.160	2.940	0.570	2.857
CESM2-WACCM	3.088	0.160	2.311	0.203	2.567
AWI-ESM-1-1-LR	3.099	0.161	2.321	0.322	2.718
EC-Earth3	3.117	0.159	3.347	0.312	3.006
NorESM2-MM	3.153	0.160	2.620	0.152	2.577
EC-Earth3-CC	3.171	0.161	3.022	0.943	3.082
MPI-ESM1-2-LR	3.180	0.160	2.795	0.209	2.722
TaiESM1	3.194	0.157	3.244	0.257	2.837
EC-Earth3-Veg-LR	3.214	0.161	3.223	0.219	3.003
CMCC-CM2-HR4	3.225	0.167	3.116	0.622	2.605
ACCESS-ESM1-5	3.248	0.160	3.686	0.623	2.838
KACE-1-0-G	3.309	0.153	3.216	0.288	2.865
NorESM2-LM	3.364	0.164	3.037	0.417	2.882
CESM2-WACCM-FV2	3.369	0.163	3.055	0.295	2.885
MPI-ESM-1-2-HAM	3.378	0.166	3.173	0.061	2.970
ACCESS-CM2	3.385	0.159	3.280	0.100	2.844
E3SM-1-0	3.408	0.156	3.632	0.186	2.776
MRI-ESM2-0	3.425	0.161	2.968	0.213	2.576
INM-CM5-0	3.425	0.159	3.182	0.423	2.902
CanESM5	3.435	0.160	3.443	0.465	3.115
FGOALS-f3-L	3.456	0.164	3.635	0.598	2.956
E3SM-1-1	3.484	0.159	3.843	0.333	2.849
CESM2-FV2	3.491	0.169	3.509	0.239	2.946
E3SM-1-1-ECA	3.503	0.161	3.611	0.374	2.899
GISS-E2-1-G	3.509	0.163	2.945	0.165	3.037
GISS-E2-1-H	3.574	0.160	3.181	0.709	2.980
CMCC-ESM2	3.576	0.156	3.643	0.516	2.820
IPSL-CM6A-LR-INCA	3.585	0.162	2.738	0.545	2.873
IITM-ESM	3.591	0.154	4.008	0.859	3.851
IPSL-CM6A-LR	3.616	0.163	2.953	0.713	2.958
INM-CM4-8	3.657	0.163	3.817	0.244	3.105
CMCC-CM2-SR5	3.664	0.155	3.883	0.626	2.884
MIROC6	3.678	0.162	3.523	1.654	3.764
BCC-CSM2-MR	3.716	0.160	3.087	1.103	3.224
GISS-E2-2-H	3.787	0.160	3.647	1.297	3.387
NorCPM1	3.794	0.166	3.464	1.493	3.756
BCC-ESM1	3.805	0.164	3.804	1.110	3.635
CAMS-CSM1-0	3.817	0.160	3.916	0.372	3.234
KIOST-ESM	3.819	0.169	3.599	0.849	3.294
IPSL-CM5A2-INCA	3.917	0.171	3.680	0.671	3.048
FGOALS-g3	4.122	0.165	4.827	1.808	4.957
NESM3	4.139	0.166	3.792	0.156	3.069
MCM-UA-1-0	5.008	0.161	4.235	0.319	3.609

Figure 10: Sliced amplitude, sliced phase, RMSE, and Wasserstein-based (Vissio et al., 2020) distances from ERA5 to NCEP and the CMIP6 model outputs for mean monthly (2m) surface air temperature. Color fill is unique to each distance metric and is calculated using ranks.

Metric comparison: CMIP6 total precipitation

	Sliced Amplitude	Sliced Phase	Sliced Translation	Vissio et al.	RMSE
NCEP Reanalysis -	5.408	0.366	1.948	0.255	2.540
CESM2 -	5.428	0.403	2.336	0.033	2.781
CESM2-WACCM -	5.521	0.406	2.170	0.013	2.812
MIROC6 -	5.772	0.407	2.575	0.269	2.861
GFDL-ESM4 -	5.775	0.417	2.449	0.050	2.849
E3SM-1-0 -	5.785	0.396	2.323	0.138	2.789
E3SM-1-1-ECA -	5.893	0.397	2.537	0.114	2.824
E3SM-1-1 -	5.895	0.399	2.401	0.129	2.798
IPSL-CM6A-LR -	5.918	0.424	2.427	0.111	2.838
IPSL-CM6A-LR-INCA -	5.950	0.421	2.252	0.116	2.848
CESM2-WACCM-FV2 -	6.004	0.402	2.440	0.027	2.895
CESM2-FV2 -	6.036	0.403	2.693	0.031	2.908
KIOST-ESM -	6.124	0.426	2.563	0.157	2.849
MRI-ESM2-0 -	6.138	0.406	2.880	0.083	2.994
KACE-1-0-G -	6.194	0.426	2.185	0.118	2.958
ACCESS-ESM1-5 -	6.255	0.404	2.730	0.291	3.085
BCC-CSM2-MR -	6.273	0.413	2.706	0.059	3.137
IPSL-CM5A2-INCA -	6.281	0.421	2.620	0.108	2.897
CanESM5 -	6.286	0.419	2.694	0.021	3.030
ACCESS-CM2 -	6.314	0.418	2.630	0.227	3.134
FGOALS-f3-L -	6.343	0.436	2.268	0.054	3.058
BCC-ESM1 -	6.370	0.419	2.531	0.118	3.254
GISS-E2-1-G -	6.569	0.417	2.394	0.081	3.152
FGOALS-g3 -	6.644	0.421	2.864	0.038	3.150
GISS-E2-1-H -	6.653	0.416	2.813	0.105	3.187
GISS-E2-2-H -	6.775	0.412	2.827	0.089	3.021
NESM3 -	7.010	0.424	2.806	0.053	2.944
MCM-UA-1-0 -	7.128	0.468	2.383	0.320	3.289

Figure 11: Sliced amplitude, sliced phase, RMSE, and Wasserstein-based (Vissio et al., 2020) distances from ERA5 to NCEP and the CMIP6 model outputs for total monthly precipitation. Color fill is unique to each distance metric and is calculated using ranks.

Metric comparison: CMIP5 surface temperature

	Sliced Amplitude	Sliced Phase	Sliced Translation	Vissio et al.	RMSE
NCEP Reanalysis	1.998	0.123	1.814	0.459	2.035
MIROC4h	3.243	0.150	2.962	0.725	2.553
MPI-ESM-MR	3.264	0.161	2.928	0.439	2.688
MPI-ESM-LR	3.284	0.160	3.069	0.272	2.702
MPI-ESM-P	3.290	0.164	3.623	0.292	2.662
ACCESS1-3	3.321	0.159	3.669	0.075	2.894
CMCC-CM	3.325	0.158	3.242	0.230	2.975
MIROC5	3.362	0.156	3.389	0.965	3.222
IPSL-CM5A-MR	3.374	0.167	3.212	0.435	2.793
NorESM1-M	3.442	0.171	3.425	0.737	3.051
MIROC-ESM-CHEM	3.477	0.150	3.563	0.254	3.120
CMCC-CMS	3.481	0.165	3.256	0.279	2.978
MIROC-ESM	3.498	0.150	3.782	0.277	3.151
IPSL-CM5A-LR	3.547	0.167	3.584	1.338	3.233
GISS-E2-R-CC	3.553	0.158	3.257	0.809	2.906
HadGEM2-AO	3.574	0.160	3.569	0.213	3.015
GISS-E2-R	3.578	0.159	3.098	0.780	2.901
ACCESS1-0	3.580	0.155	3.410	0.189	2.941
HadGEM2-ES	3.583	0.160	3.993	0.460	3.065
CNRM-CM5	3.608	0.156	3.134	0.221	3.008
CanESM2	3.610	0.162	4.176	0.460	3.241
NorESM1-ME	3.671	0.167	3.275	1.138	3.365
GISS-E2-H-CC	3.754	0.161	2.991	1.080	3.033
HadGEM2-CC	3.765	0.161	3.534	0.768	3.318
GFDL-CM3	3.772	0.170	4.195	0.357	2.806
CanCM4	3.782	0.160	3.797	0.236	3.189
CNRM-CM5-2	3.820	0.158	3.580	0.535	3.201
GISS-E2-H	3.846	0.164	3.543	1.463	3.381
inmcm4	3.953	0.179	3.688	0.342	3.440
CMCC-CESM	3.969	0.179	3.911	0.220	3.507
MRI-ESM1	4.084	0.167	4.201	0.210	3.053
MRI-CGCM3	4.088	0.169	4.328	0.102	3.073
GFDL-ESM2M	4.180	0.170	3.179	0.107	3.134
GFDL-ESM2G	4.220	0.165	3.876	0.593	3.257
HadCM3	4.229	0.169	3.737	0.964	3.759
CSIRO-Mk3-6-0	4.234	0.171	4.069	0.857	3.612
GFDL-CM2p1	4.255	0.165	3.242	0.656	3.093
IPSL-CM5B-LR	4.322	0.165	5.028	0.856	4.113
FGOALS-s2	4.322	0.164	3.921	1.138	3.723

Figure 12: Sliced amplitude, sliced phase, RMSE, and Wasserstein-based (Vissio et al., 2020) distances from ERA5 to NCEP and the CMIP5 model outputs for mean monthly (2m) surface air temperature. Color fill is unique to each distance metric and is calculated using ranks.

Metric comparison: CMIP5 total precipitation

	Sliced Amplitude	Sliced Phase	Sliced Translation	Vissio et al.	RMSE
NCEP Reanalysis -	5.408	0.366	2.075	0.255	2.540
MIROC5 -	5.881	0.411	2.612	0.307	2.804
CanCM4 -	5.913	0.406	2.236	0.127	2.813
MIROC-ESM-CHEM -	5.970	0.408	2.376	0.118	2.741
CanESM2 -	5.986	0.415	2.545	0.138	2.859
ACCESS1-0 -	6.014	0.418	2.653	0.160	3.071
MIROC4h -	6.019	0.408	2.495	0.052	2.878
MIROC-ESM -	6.051	0.416	2.333	0.103	2.747
HadCM3 -	6.174	0.405	2.615	0.023	2.995
inmcm4 -	6.176	0.409	2.422	0.261	2.822
IPSL-CM5A-LR -	6.184	0.427	2.450	0.197	2.759
CNRM-CM5 -	6.266	0.408	2.148	0.159	2.694
IPSL-CM5A-MR -	6.269	0.439	2.644	0.116	2.821
CNRM-CM5-2 -	6.273	0.405	2.200	0.128	2.685
GISS-E2-R-CC -	6.300	0.412	2.658	0.273	2.991
GFDL-ESM2G -	6.301	0.406	2.881	0.055	2.992
GFDL-CM2p1 -	6.324	0.399	2.948	0.029	3.071
GISS-E2-R -	6.333	0.410	2.676	0.274	3.000
NorESM1-ME -	6.357	0.412	2.560	0.121	2.836
HadGEM2-ES -	6.369	0.420	2.552	0.147	3.047
HadGEM2-CC -	6.369	0.413	2.414	0.121	3.030
ACCESS1-3 -	6.400	0.410	2.813	0.245	3.051
FGOALS-s2 -	6.401	0.426	3.065	0.152	3.059
HadGEM2-AO -	6.427	0.413	2.574	0.184	3.087
MPI-ESM-P -	6.462	0.419	2.722	0.043	3.058
MPI-ESM-LR -	6.476	0.421	2.860	0.052	3.069
NorESM1-M -	6.529	0.418	2.620	0.101	2.873
CMCC-CM -	6.538	0.427	2.585	0.010	3.107
GFDL-ESM2M -	6.542	0.399	2.845	0.074	3.090
MPI-ESM-MR -	6.562	0.421	3.011	0.100	3.100
GISS-E2-H-CC -	6.581	0.419	2.876	0.311	3.204
CMCC-CMS -	6.585	0.425	2.843	0.028	3.115
GFDL-CM3 -	6.616	0.402	2.605	0.092	2.935
GISS-E2-H -	6.620	0.416	2.917	0.316	3.190
CMCC-CESM -	6.750	0.427	2.913	0.011	3.146
CSIRO-Mk3-6-0 -	6.758	0.409	3.067	0.016	3.282
IPSL-CM5B-LR -	6.814	0.446	2.779	0.111	3.190
MRI-ESM1 -	6.875	0.431	2.993	0.040	3.197
MRI-CGCM3 -	7.026	0.436	3.166	0.027	3.191

Figure 13: Sliced amplitude, sliced phase, RMSE, and Wasserstein-based (Vissio et al., 2020) distances from ERA5 to NCEP and the CMIP5 model outputs for total monthly precipitation. Color fill is unique to each distance metric and is calculated using ranks.